



---

# Rutherford Scattering measurements with SSB and ALPIDE detectors

Ardino Rocco	Mat. 1231629	<a href="mailto:rocco.ardino@studenti.unipd.it">rocco.ardino@studenti.unipd.it</a>
Bortolato Gabriele	Mat. 2019062	<a href="mailto:gabriele.bortolato@studenti.unipd.it">gabriele.bortolato@studenti.unipd.it</a>
Valente Alessandro	Mat. 1234429	<a href="mailto:alessandro.valente.4@studenti.unipd.it">alessandro.valente.4@studenti.unipd.it</a>

(Dated: February 16, 2021)

In this work we discuss the construction of an experimental apparatus for Rutherford Scattering measurements. In particular, we treat in detail each module of its composite structure and we present the operations done for their characterisation. Moreover, we treat the implementation of a numerical simulation to model with first order approximations the apparatus and we compare the experimental data for the angular scattering distribution with the expected results. Lastly, we give statistical significance to the results through several standard test statistics and we discuss the agreement between theory and experiment.

---

## CONTENTS

I. Introduction	1
II. Experimental apparatus	3
1. Vacuum system	3
2. Mechanical system	4
3. Radioactive source	6
4. SSB detection system and electronics chain	7
5. ALPIDE detection system	9
6. Internal network	11
III. Setup characterisation and preliminary tests	12
1. SSB detector characterisation	12
2. ALPIDE detector characterisation	13
3. Radioactive source characterisation	17
4. Simulation of the apparatus	19
5. Characterisation of beam profile and validation of simulation	21
IV. Experimental data analysis and results	22
1. Data acquisition planning	22
2. Scattering angular distribution	23
3. Statistical analysis	23
4. Discussion of results	26
V. Conclusions	27
References	28

---

## I. INTRODUCTION

**a. Background of the experiment** In the beginning of the 20<sup>th</sup> century, the study of the structure of atoms began to intensify. In particular, J.J. Thomson, after the discovery of electrons, hypothesised the “plum pudding” model: the structure of the atom consists of electrons occupying a region of space uniformly and positively charged. Ernest Rutherford tested if this behaviour of nature was plausible and set up his famous experiment, proving that Thomson’s prediction could not explain the experimental data. His idea was to study the atomic structure through scattering experiments, namely bombarding a thin gold target with  $\alpha$  particles projectiles. This was the start of a revolution, since with the experimental data he obtained he was finally able to solve a long standing riddle by introducing a new hypothesis. It was the birth of the Rutherford model, where the positive charge is densely-packed in the atom centre, forming the nucleus.

**b. Scattering processes in a nutshell** Returning to the present time, a general scattering process is typically described in terms of the differential cross section. This is nothing more than a function describing the probability of a scattering event to occur. In the particular case of a charged particle as projectile going against a nucleus target, the differential cross section according to Rutherford description reads:

$$\frac{d\sigma}{d\Omega} = \left( \frac{ZZ'e^2}{16\pi\varepsilon_0\mathcal{E}} \right)^2 \frac{1}{\sin^4 \frac{\theta}{2}}, \quad (1)$$

where:

- $Z$  and  $Z'$  are the atomic numbers of the incoming particle and of the scattering material, respectively;
- $e$  is the unit charge, namely the charge of a proton;
- $\mathcal{E}$  is the energy of the incoming particle;
- $\theta$  is the polar angle at which the incoming particle scatters with respect to the scattering centre, namely the atom nucleus.

However, the expression given in EQ. 1 is only an approximation given by a simplified model and naive geometrical hypotheses. In fact, for small angles it diverges, which is in contrast with the experimental observations. For instance, in a real experiment we do not deal with beams with a point-like section or monochromatic spectrum. They have a more complex shape that should be modelled and the energy of their particles is dispersed. Every of these details induces a small correction to the already known result, but their joint contribution leads to discrepancies with theoretical expectations.

**c. Aims of the work** Given the premises on which the following discussion will hold on, in this work we try to reproduce Rutherford’s experimental work and to extrapolate the results on the differential cross section of the scattering process with a regard towards the various corrections due to both geometry and inner physics. More in particular, our aims are in logical order to:

- elaborate and describe an appropriate experimental setup for performing measurements of charged particles scattering;
- characterise the instruments employed for the measurements;
- model through numerical simulations the components of the apparatus and the physics of the phenomenon under study;
- extract the angular scattering profile distribution of the physical process from the analysis and compare it with the expected results from simulation.

Due to the shorter time at our disposal for the exceptional situation of 2020, the activity would have come to completely different results without the heredity of previous iterations of the experience. Several technical realisations have been taken from them, in particular:

- the supports for the  $\alpha$  source and the silicon detector;
- the collimators of the beam;
- the mechanics and electronics for the motor control;

- the software for the acquisition from the silicon detector.

On the other hand, several improvements and new systems have been introduced in this iteration, including:

- a new ALPIDE pixel detector for the acquisition, with a finer geometrical resolution, along with its support and the software needed to control it from an FPGA;
- an improved configuration for the mechanical system of the motor, in order to perform acquisitions with both the detectors contemporaneously in the vacuum chamber;
- a new simulation of the apparatus and of the physics of the scattering process;
- several small improvements to the entire setup, including the possibility to perform all the operations for data acquisition in remote.

## II. EXPERIMENTAL APPARATUS

In this Section we describe the experimental apparatus designed for the experience, focusing in particular to the new improvements made with respect to the previous years iterations. The structure of the setup is characterised by its modularity. In fact, we can distinguish several connected sections, in particular:

- a **radioactive source** of  $^{241}\text{Am}$ , with the active material inside an aluminium cylinder. The overall structure of this piece is inlaid in a 3d-printed support;
- a **vacuum system**, including a vacuum chamber, a pumping station to reach the vacuum condition and two vacuum gauges to keep track of the internal pressure of the chamber;
- a **mechanical system**, including a step motor through which the support of the source is rotated. This is connected to an Arduino shield tower and to a computer, through which the step position can be regulated;
- a set of **thin foils** of different materials, such as gold and tin, on which the  $\alpha$  particles can scatter;
- a partially depleted **Silicon Surface Barrier (SSB) detector**, connected to a NIM module electronics chain and then to a PicoScope digital oscilloscope acting as digitizer, in order to sample the waveforms of the candidate  $\alpha$  signals;
- an **ALice PIXel DEtector (ALPIDE)**, whose acquisition is managed by a Field Programmable Gate Array (FPGA) with a dedicated firmware;

Hereafter we describe each of these components in detail, starting from the inner core of the apparatus, namely the vacuum system, and finally coming to the two independent detection systems with SSB and ALPIDE detectors, respectively. In addition, we also discuss about a configuration of the Local Network Area in our apparatus in order to improve the capabilities of remote control of the acquisitions.

### 1. Vacuum system

**a. Vacuum chamber** The core component of the vacuum system, in which the scattering process takes place, is the vacuum chamber. It has a cylindrical form and its internal diameter is of about 22 cm. It has several gateways on its side surface, where the so-called feedthroughs can be placed to transfer all the electronic signals outside the chamber. The whole chamber is showed in FIG. 1a.

**b. Pumping station** One of the gateways is dedicated to the connection to the pumping station Pfeiffer Vacuum HiCube-80, showed in FIG. 1b and versatile for all high and ultrahigh vacuum applications [1]. The latter is composed of a diaphragm pump and a turbomolecular pump. Their operations during their working are automated: firstly, the diaphragm pump will produce low vacuum, then the turbomolecular will slowly reach its regime and produce the high vacuum needed. To lower the stress to the turbomolecular pump, two pipes in the middle of the station and the chamber are inserted, with different magnitudes of conductance. The higher conductance pipe has an on-off valve type, while the low conductance one has a variable valve to tune its conductance. These are showed in FIG. 1c.

**c. Gauges, valves and working point** When making the vacuum, two independent gauges monitor the pressure in the vacuum system. The first one, namely a **Penning** gauge, is placed in the chamber and it gives information on the internal pressure of the apparatus. The second one, namely a **Pirani** gauge, is placed just after the turbomolecular pump in order to signal an eventual stress to the turbine when the variable valve impedance is excessive. Moreover, a third variable valve is placed right before the turbomolecular pump in order to break the vacuum slowly and preserve sensible devices inside the chamber, such as the target foils.

A complete setup of the vacuum valves is showed in FIG. 1c. Through this whole vacuum setup, it is possible to reach the working point pressure for this experiment:

$$p = (9.0 \pm 0.2) \cdot 10^{-5} \text{ mbar} . \quad (2)$$

This is sufficient to perform a scattering experiment with the required precision of measurements. In fact, the loss of energy due to the residual molecules of air in the chamber can be reasonably neglected with respect to the losses due to other factors, treated in the following Subsections.

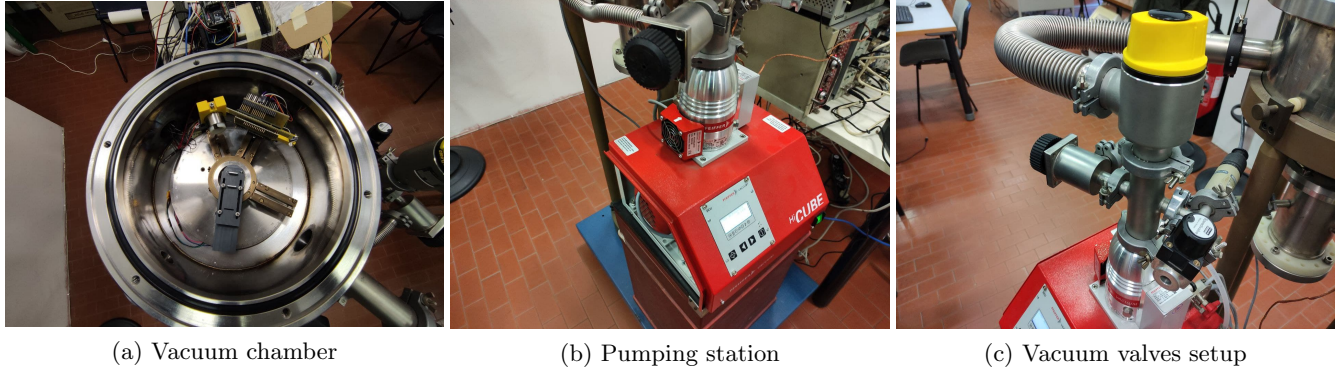


**FIG. 1** Vacuum chamber employed for the experiment in **1a** and pumping station Pfeiffer Vacuum HiCube-80 in **1b**. In **1c**, the whole vacuum valves setup.

## 2. Mechanical system

**a. Step motor** Again, we start from the core component of this section of apparatus, namely the step motor, showed in FIG. **2a**. It is hidden at the very bottom of the vacuum chamber and it allows to modify the angle of the source beam direction with respect to the detectors positions. More in particular, the step motor is a 4-cable type with two sets of active coils, through which its revolution is divided into 400 steps. Therefore, the angular interval covered in a single step rotation is equal to:

$$\Delta\theta_{\text{step}} = (0.9 \pm 5\%) \text{ deg} \quad . \quad (3)$$

In order to control the step motor from a computer, an Arduino microcontroller is exploited. In particular, this part includes also two overlying shields, designed in a previous iteration of the experience and translating the Arduino digital signals in actual impulses for the motor. Moreover, the shields are connected to two microswitches placed at the edges of the detection system to define the angular boundaries needed to perform an angular calibration of the motor. One of them is showed in FIG. **2c**.

**b. Source support and collimators** A 3d-printed plastic support for the radioactive source is directly connected to the shaft of the motor, so that it can rigidly rotate with the motor itself. This piece is showed in FIG. FIG. **2b**, where we can observe its composite shape with two grooves. The ladders are designed to securely accommodate the two collimation targets. Moreover, on its final part, in front of the last collimator, there are two threads on which the scattering foil can be locked through two screws.

Concerning the collimators, these are nothing more than aluminium targets with an engraved groove, whose width  $c_1$ , height  $c_2$  and thickness  $c_3$  are listed in TAB. **I** along with the distance  $d_{\text{cc}}$  between the two collimators. A picture of a sample of this component is showed in FIG. **2d**.

Dimension	Symbol	Length [mm]
Groove width	$c_1$	4.0
Groove height	$c_2$	7.0
Groove thickness	$c_3$	1.3
Groove-Groove distance	$d_{\text{cc}}$	20.0

**TAB. I** Relevant physical dimensions for the two collimation targets, in particular for their grooves and their reciprocal distances, which are of crucial importance for a correct modelling of the apparatus.

**c. Detectors supports** The SSB detector support is made of a metallic frame and a plastic structure in which one of the microswitches is fixed. The metallic frame consists in a base connected to a rail over the base of the vacuum chamber, and a hollow cylinder housing the detector. The latter is collimated with a metallic annular target, whose groove diameter length is 4 mm. The latter is necessary to perform finer angular measurements for a fixed position. The overall support is showed in FIG. **2e**.

On the other hand, the ALPIDE support is a simple 3d-printed base inserted in an another rail of the chamber. On this polymer structure, a PCB is fixed and some pins are soldered on it for the needed ALPIDE shield connections. Again, the structure of the support is showed in FIG. 2f, where we can also observe the second last microswitch fixed on the plastic base.

The distances of both the supports from the centre of rotation of the motor are measured indirectly through angular measurements with the aim of a laser. It is possible to do this with high precision since the dimensions of ALPIDE and SSB detectors supports are known with a negligible uncertainty. So, given the angular extension  $\Delta\theta$  of the support of the SSB or of ALPIDE detector and their length  $\ell$ , we can extract the distance  $d$  with simple calculations:

$$d = \frac{\ell}{2} \tan^{-1} \left( \frac{\Delta\theta}{2} \right) . \quad (4)$$

We report the results for the distances from the supports in TAB. II.

Component	$d$ [mm]
ALPIDE detector	$78.6 \pm 0.7$
SSB detector	$92 \pm 1$

**TAB. II** Distances of the two detectors with respect to the centre of rotation of the motor, coinciding with the centre of the vacuum chamber.

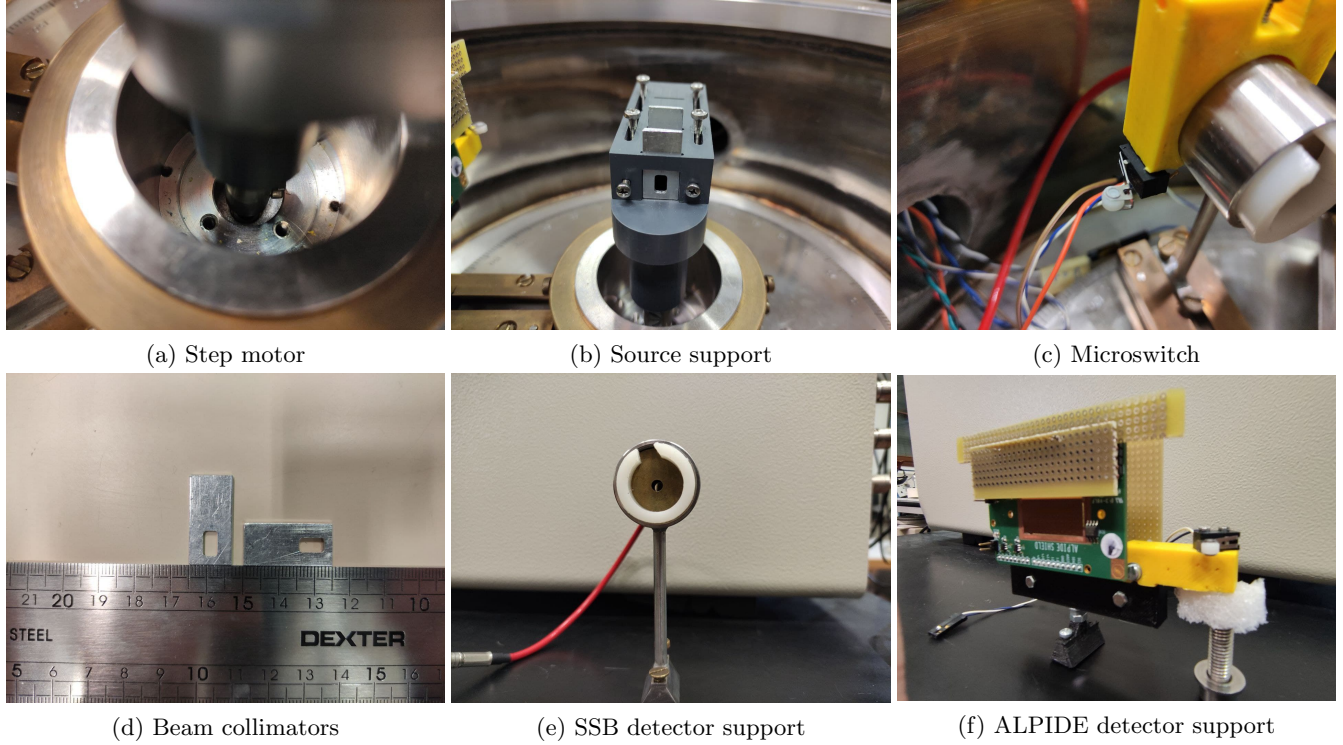


**FIG. 2** Components of the mechanical system of the experimental apparatus.

**d. Scattering foils** For the measurements of  $\alpha$  particles scattering on a target, a set of thin foils of gold and tin are employed. These are characterised by a very small thickness, so they must be handled with great care when placing them in face of the source support, on which they are fixed through two screws. In particular, the specifics of the foils are given in TAB. III.

Foil material	$\rho_{\text{sup}}$ [ $\mu\text{g}/\text{cm}^2$ ]	$\rho$ [ $\text{g}/\text{cm}^3$ ]	Thickness [ $\mu\text{m}$ ]
gold	325	19.32	0.168
tin	500	7.29	0.686

**TAB. III** Specifics of the scattering foils employed for the experiment, in particular the superficial density, the volume density and the thickness are reported in columnar order.

### 3. Radioactive source

The radioactive  $\alpha$  source employed for the experiment is schematized in FIG. 3a [3]. The active material inside it is a layer of  $^{241}\text{Am}$ , covered by two consecutive thin layers of gold. These parts are inserted inside an aluminium support, whose diameter and length are about 12 mm and 79 mm, respectively, and it is schematised in FIG. 3b. A complete list of the relevant radiations and particles emitted by this source is given in TAB. IV [4]. As we can see, we do not have only particles originated from  $\alpha$  decay, but also X and  $\gamma$  rays emissions. These are not a big deal for the SSB detector due to its working principles, but they constitute a relevant background for ALPIDE detector and special data analysis and statistical techniques should be employed, as we will see in the following Sections.

Emission	Energy [keV]	Weight
$\alpha$	5485.56	84.45
$\alpha$	5442.80	13.23
$\alpha$	5388.25	1.66
$\gamma$	59.5	35.92
X	11.9 $\div$ 22.2	37.66

**TAB. IV** Relevant emissions of the employed  $^{241}\text{Am}$  source along with the corresponding energy. Concerning the weight, it should be intended as a probability of emission, for the  $\alpha$  decay mode, or as a number of photon emissions per 100 disintegrations, for the X and  $\gamma$  modes.

Concerning the actual activity, it can be calculated knowing that in October 2019 it was  $\dot{N}(t_{2019 \text{ Oct}}) \approx 368.0 \text{ kBq}$ , as declared in [2]:

$$\dot{N}(t_0) \approx \left(\frac{1}{2}\right)^{\frac{\Delta t}{t_{1/2}}} . \quad (5)$$

Therefore, knowing the half-life of  $^{241}\text{Am}$ <sup>1</sup> and the temporal interval  $\Delta t$  from the last activity measurement to October 2020, we can approximate the source activity during the 3 months experimental measurements:

$$\dot{N}(t_0) \approx 367.4 \text{ kBq} . \quad (6)$$

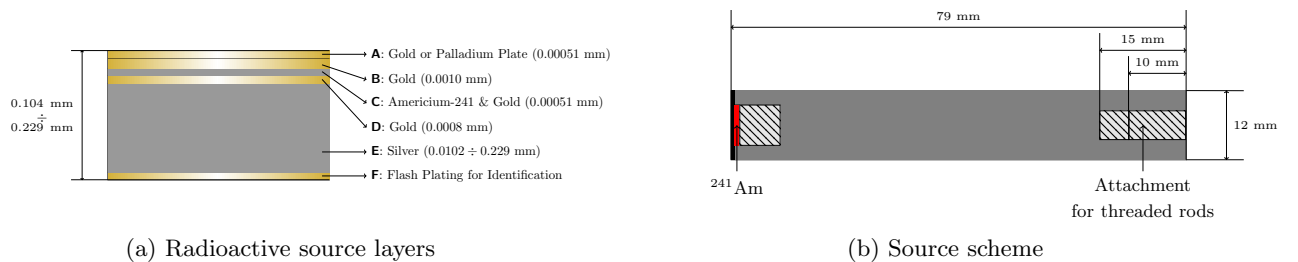


**FIG. 3** Radioactive source schemes of the layers covering the active material of  $^{241}\text{Am}$  in 3a and of the overall structure of the aluminium cylinder support in 3b.

<sup>1</sup>  $t_{1/2} = 432.14 \text{ y}$ .

#### 4. SSB detection system and electronics chain

This part of the apparatus is composed of multiple modules. In this Subsection we briefly describe it briefly step by step. So, we have in logical order:

- an ORTEC SSB Series A silicon detector, placed on an apposite support inside the vacuum chamber and interfaced to the external side of the chamber by a microdot-to-BNC connector;
- a Canberra 2003BT preamplifier, connected directly to the BNC interface in order to reduce the noise propagation along the electronics chain;
- a set of NIM modules for multiple purposes, including a polarizer, a shaping amplifier and a scaler for a raw real-time counting of the events detected by the silicon;
- lastly, a PicoScope 5000 oscilloscope working as a digitizer of the analogue signal coming from the amplifier. This block is connected to a computer which controls both the mechanical and the acquisition systems.

**a. ORTEC SSB silicon detector** The first element of the chain is a so-called **partially depleted Silicon Surface Barrier (SSB)** detector, produced by ORTEC and with serial model A-035-025-300 [5]. A simple scheme of its structure is illustrated in FIG. 4, where the values of the geometrical parameters are:

$$x = 16.7 \text{ mm} \quad (7)$$

$$y = 12.3 \text{ mm} \quad (8)$$

$$z = 7.1 \text{ mm} \quad (9)$$

$$w = 5.6 \text{ mm} \quad (10)$$

Therefore, the active area of the detector is about  $25 \text{ mm}^2$ . Concerning the rear part of the component, it has not a standard BNC connector, but a Microdot one. As given by the specifics of construction, the minimum depletion depth is  $300 \mu\text{m}$ , while the guaranteed maximum resolution is approximately 35 keV.

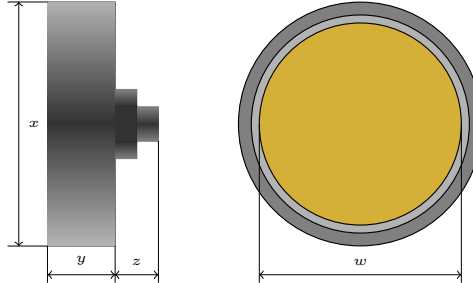


**FIG. 4** ORTEC A-035-025-300 scheme with lateral and frontal views. The geometrical dimensions of the component are explicitly indicated and their values are given in EQS. 7-10.

**b. Canberra 2003BT preamplifier** The Model 2003BT charge sensitive FET input preamplifier is employed due to its optimum performance with SSB detectors, as suggested by the user manual [6]. Operating as a charge to voltage converter, the unit accepts charge carriers produced in the detector during each absorption event. Then, the output provides a voltage in direct proportion to the collected charge. For typical use with positively biased SSB detectors, an extremely linear energy output provides a positive polarity pulse which can be exploited for energy spectroscopy. The coincident timing output provides a negative polarity fast differentiated pulse, which allows to improve the resolution of the events in time.

The basic operation of the preamplifier is indicated in the functional schematic in FIG. 5. The first stage acts as an operational integrator, which produces an output potential proportional to the accumulated charge on the feedback capacitor  $C_f$ . The integrator drives the energy output directly. The timing output is derived from the integrator error signal through a pulse shaping network. Such an arrangement lowers the noise level and gives faster rise times. To preserve pulse fidelity, the energy output is buffered through a series terminating resistor of  $93 \Omega$ .

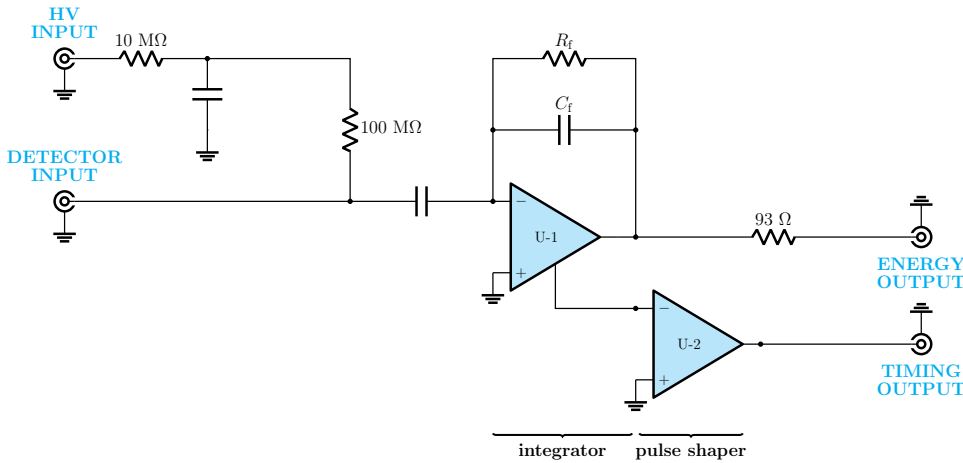


**FIG. 5** Canberra 2003BT preamplifier circuit schematic, divided into a stage integrating the collected charge (proportional to energy output) and a final pulse shaper section for timing output.

**c. NIM modules** The next stage where an event signal detection goes through is the NIM modules rack. Going in order, the first one is a polarizer of the SSB detector, set at a  $\sim 100$  V bias in order to be sure that the silicon wafer of the detector is sufficiently depleted but also not in the breakdown region. In fact, this would cause severe damages to the detector due to a rapid increase in the leakage currents.

The second NIM employed, whose input is directly connected to the preamplifier output, is the Canberra Model 2024 Fast Spectroscopy Amplifier [7]. This near-Gaussian filter shaping is optimised to improve the pulse symmetry and to get minimum sensitivity to variations in detector rise time and maximum signal-to-noise ratio. Unipolar shaping is achieved with one differentiator and two active filter integrators and offers six front panel switch selectable pulse shaping time constants.

The 2024 model includes also a Gated Integrator to reduce spectrum broadening at the shorter amplifier shaping time constants. This component integrates the entire unipolar signal, providing a properly scaled linear output signal without the resolution degrading problems normally associated with fast amplifier shaping times and long detector charge-collection times.

**d. PicoTech PicoScope 5244B digital oscilloscope** This is the last part of the silicon detection system, employed as digitizer of the shaping amplifier output signal [8]. It has memory storage of 256 MS (Mega-Samples) and it can be divided into more segments. The ensemble of the segments forms a block.

In the context of the experiment, the PicoScope is connected to a computer through USB cable and the operations done by the digitizer are the following, in chronological order:

- the memory is firstly reset and zeroed, then it is divided into the number of segments required by the user;
- the trigger chosen by the user is set;
  - every time the trigger is activated, the  $i^{\text{th}}$  segment is populated with the samples acquired;
  - after having filled the  $i^{\text{th}}$  segment, the  $(i + 1)^{\text{th}}$  segment is filled...
  - ...and so on and so forth, until the last segment is filled;
- PicoScope driver downloads the whole content of the memory on the computer and the cycle restarts.

It is important to remark that in these operations PicoScope sets the trigger once in a cycle, before starting to fill the segments. This operation constitutes a dead-time of about  $\sim 10 \mu\text{s}$ . This is crucial when the expected rate of acquisition is high and in this case it is convenient to divide the memory block in a sufficient number of segments. On the other hand, when dealing with low rates, it becomes convenient to divide the memory into a single segment, so that every event constitutes a block. In fact, in this case the dead-time due to the reset of the trigger can be neglected.

**e. Control software** The software needed to control both the mechanical system and the PicoScope is written in Python, using the library “wx” for the handling of the GUI. After running the executable, the user can choose several commands in two sections, one for the motor and one for the PicoScope. In particular, it is possible to calibrate the motor, enable it and choose the step position. On PicoScope side, it is possible to change the acquisition parameters, such as the acquisition time, the trigger value in mV, the number of segments, the events to acquire and the sample rate.

## 5. ALPIDE detection system

Also this detection system has a modular structure, but with a lower number of blocks with respect to the SSB detection system discussed above. In fact, ALPIDE detection system includes in logical order:

- an ALPIDE chip mounted on the apposite support, placed inside the vacuum chamber and interfaced to an external FPGA;
- an Arty-A7 board, equipped with an Artix-7 FPGA;
- a NUC computer to provide the communications with the FPGA through the IPBus suite.

**a. ALPIDE chip** The ALPIDE sensor is developed for the ALICE Inner Tracking System (ITS). It is a **Monolithic Active Pixel Sensor (MAPS)**, where a collection diode and the readout electronics share the same monolithic silicon die, as it is schematised in FIG. 6. This layout simplifies the connection between detectors and relative amplifiers. The detection area is arranged in a  $1024 \times 512$  pixel matrix with a  $30 \times 15 \text{ mm}^2$  form factor, where each pixel has its own analogue and digital chain, showed in FIG. 7.

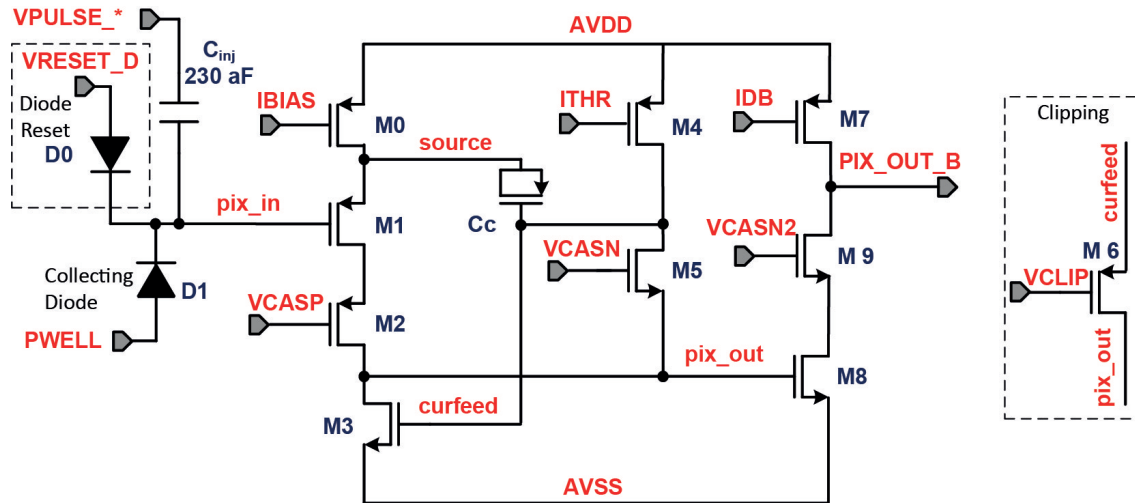


**FIG. 6** ALPIDE analogue frontend. D1 is the collection diode, M1 and M2 are a cascode preamplifier, M4 and M5 are the discriminator where the values of ITHR and VCASN parameters can be modified to change the firing threshold value for  $n_{\text{electrons}}$ .

The pixels are organised in double columns, which communicate to the control register through a priority encoder. The latter gives an address to each pixel and this is used to mask, pulse or read the state of a single pixel or a group of them through specific registers.

ALPIDE communicates with the DAQ system through two ports: the **CTRL port** (slower, 40 Mbps) and the **Data port** (faster, up to 1.2 Gbps). However, our PCB allows only the access to the CTRL port. This implies a limitation on the readout speed and so on the maximum event rate of acquisition. Its protocol is described in the ALPIDE user manual [10]: the FPGA sends a command for reading or writing, the address of target register and eventually the data to write. This has some similarities to the I<sup>2</sup>C protocol.

**b. Data acquisition firmware** The FPGA board employed for the experiment is the XC7A35TICSG324-1L Arty A7 [12]. Its original firmware was developed in a previous work [13] and it has been modified to fit our needs.

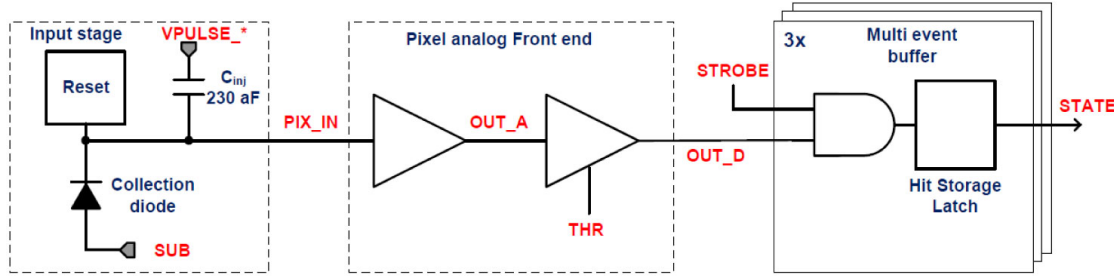


**FIG. 7** ALPIDE pixel signal chain. Some functionalities are highlighted, such as the so-called strobing, which acts as enable for storage latches, and the memory registers, 3 for each pixel.

It consists in various state machines to decode (receiver functionality) and encode (transmitter functionality) the commands that come from or go to ALPIDE shield. The system is timed by an internal clock of 40 MHz, generated by a Mixed-Mode-Clock-Manager (MMCM)<sup>2</sup> inside the FPGA. This clock reference is also propagated to ALPIDE detector.

The most important routines available in the framework are:

- **initialisation (init)**: it writes some specific registers to reset and set the chip in a predefined state;
- **read register (rr)**: it reads a specific register;
- **write register (wr)**: it writes a data on a specific register;
- **continuous readout (rope)**: similar to the read register routine but it reads continuously two registers that are associated to the data stored in the ALPIDE data FIFO.

Several debug features are implemented in the FPGA as well, such as the status LEDs (“power on”, “initialisation done” and “busy” states) and error LEDs. Moreover, it is implemented with a suite that communicates with the PC, namely the IPBus suite [14]. This consists in various modules that connect the programmable logic available in the FPGA fabric to the ethernet controller, which sends and receives data from PC. The latter translates the ethernet packets exploiting the *μhal* Python and C++ library.

The connection to the ALPIDE shield is made of eight cables, showed in FIG. 8a and FIG. 8b and listed in FIG. 8c.

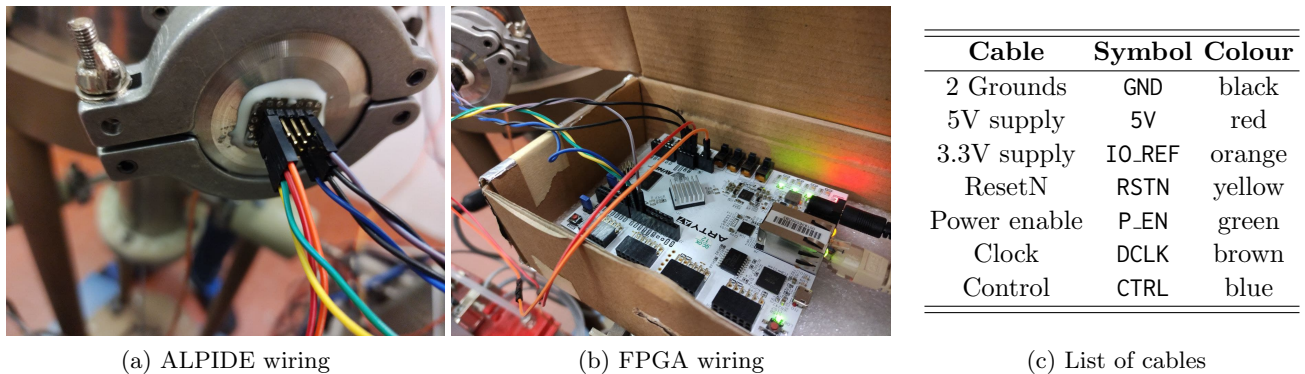


**FIG. 8** ALPIDE connections to the feedthrough in 8a, to the FPGA in 8b and list of their functionalities and corresponding colours in 8c.

**c. PC readout** The readout and the ALPIDE control are performed by a Command Line Interface coded in Python 2.7. It allows to exploit some basic functionalities of the chip, such as power on/off ALPIDE, read/write registers and the most important one, namely the continuous readout.

<sup>2</sup> Similar to a PLL (Phase Locked Loop), but with some advanced features

ALPIDE has its own communication protocol and to read the data from the control port it necessary to extract the value from two specific registers, DMU\_Data\_FIFO[15:0] (0x12) and DMU\_Data\_FIFO[23:16] (0x13). This read method implies a serious limitation on the effective throughput. In fact 218 clock cycles are necessary to read a single 24 bit data. This fact translates to an effective throughput of 4.404 Mbps. On the other hand, the two high speed ports can reach a throughput of 320 Mbps (parallel) and 960 Mbps (serial with 8b/10b encoding).

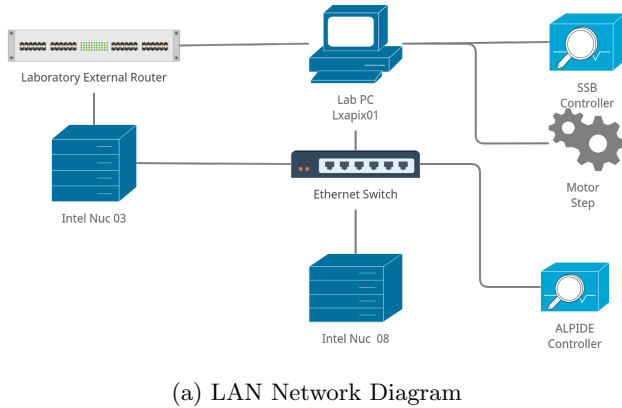
The effective throughput obtained in real data acquisition is 4.304 Mbps. It is important to highlight in this context that the DMU (Data Management Unit) sends the acquired data in a packet format, described in the ALPIDE User Manual [10]. Knowing these informations, it is possible to evaluate the time needed to read a single  $\alpha$ -cluster which has a mean area of about 30 pixels:

$$r_{\text{cluster}} = \sqrt{\frac{\text{Area}_{\text{cluster}}}{\pi}} \approx 3 \text{ px} . \quad (11)$$

This means that we have at least 3 double columns registers for event. Enabling the compression of data in clusters (up to 8 adjacent pixels on a single 24bit data), we have a minimum of 6 data samples. Adding also the data formatting (Chip Header, Chip Trailer and 2 Region Header) we get a total of 10 data, which become 18 considering at least 2 additional noise pixels. These data samples correspond to a total of 3194 clock cycles (at 40 MHz) or about 100  $\mu\text{s}$ . So, this detection system can stand a maximum theoretical rate of  $10^4$  ev/s. However, this limit is lowered by the drawbacks of using the slow port: the ALPIDE FIFO overflow. In fact, the memory has a depth of 64 locations, so there is a limit of about 3  $\alpha$ -clusters stored before the assertion of a critical readout flag.

## 6. Internal network

In order to produce statistically significant results, long acquisition times are required. This fact, alongside with the necessity of monitoring the system during acquisition, makes necessary the possibility of controlling the whole setup from a remote location. To do this, we employ a switch to create a Local Area Network, which allows us to connect and control the two detectors and the step motor through an ssh connection. In FIG. 9a the network setup is showed, while in TAB. 9b its nodes are listed.



(a) LAN Network Diagram

IP	Device
10.10.10.2	Lab PC laxpix01
10.10.10.20	Intel NUC 08 Mini PC
10.10.10.30	Intel NUC 03 Mini PC
10.10.10.100	ALPIDE Controller

(b) IP Addresses of the LAN nodes

**FIG. 9** Network diagram for the LAN setup in 9a, where the main components for the remote monitoring are explicitly remarked. In 9b, a list of the IP addresses corresponding to the main devices.

As we can see from TAB. 9b, the step motor and the Arduino controller are not present, since these are controlled from the laboratory PC via USB connection. So, a total number of three computers is present inside the network: one for motor and SSB detector control, another one for ALPIDE detector control, and the last one for simultaneous control of both the acquisition systems.

### III. SETUP CHARACTERISATION AND PRELIMINARY TESTS

Before switching to the discussion of the acquisition and data analysis, we present the preliminary operations performed to characterise the apparatus. These are needed in order to improve the quality of the final measurements and to refine the analysis strategy as well as the approximations for a sufficiently simple but correct simulation. So, in this Section we discuss:

- the characterisation of the SSB detector, including the meaningful information that can be extrapolated by the acquired waveforms in order to discriminate the background;
- the characterisation of ALPIDE detector, which constitutes a more delicate operation due to the kind of data acquired and to its working principles. In particular, a crucial aspect on which we will stress more attention is the X-ray background discrimination;
- the radioactive source characterisation, including the calculations to extrapolate the  $\alpha$  particle energy exiting from the gold protection foils, the uniformity of emission and the energy correlation with the angle of emission;
- before passing to the characterisation of the beam profile, we discuss a Python based numerical simulation through which we model the apparatus, the  $\alpha$  particles beam and the physics of scattering on the thin foils;
- lastly, we treat the beam characterisation by comparing the experimental data acquired without the scattering foil inserted in the relative support and the expectation obtained by the numerical simulation.

#### 1. SSB detector characterisation

**a. Waveform analysis strategy** A first preliminary analysis is done by performing a test acquisition with the detector placed at an angular position of 0 deg with respect to the beam line, setting the threshold trigger at 500 mV and with a time resolution of 12 bits and a sample rate of 200 MS/s. With this choice of sample parameters, each acquired waveform can be represented by a set of points  $(t_i, y(t_i))$ , with  $t_i = 0, \dots, 4999$ . An example is showed in FIG. 10a, where the waveform has been smoothed with a moving average filter. As we can see:

- the baseline of the signal spaces the region  $\mathcal{B} = \{t_i \lesssim 1000\} \cup \{t_i \gtrsim 3000\}$ ;
- the peak spaces the range  $\mathcal{P} = \{1000 \lesssim t_i \lesssim 3000\}$ .

Therefore, we calculate the baseline  $b$  with a simple average in the baseline region  $\mathcal{B}$ . Now, knowing that the energy  $\mathcal{E}$  of the detected particle is proportional to the integral of the collected charge, we compute  $\mathcal{E}$  by simply integrating the waveform and subtracting the baseline:

$$\mathcal{E} \propto \int_{t_i}^{t_f} Q(t) dt \propto \sum_{i=i_0}^{i_f} y(t_i) - b(t_f - t_0) \quad , \quad (12)$$

where  $t_f = 4999$  and  $t_0 = 0$ . The histogram reporting the integrals for the test run is showed in FIG. 10b.

Another important quantity that can be extracted from the waveforms, useful for background discrimination, is the amplitude in mV. This can be easily estimated by subtracting the baseline  $b$  from  $\max\{y_i\}$ :

$$\Delta V = \max\{y(t_i)\} - b \quad . \quad (13)$$

We show the histogram for this quantity for the test run in FIG. 10c.

**b. Background discrimination strategy** When dealing with low signal rates, namely when acquiring at a sufficiently large angular position with respect to the beam direction, it becomes of paramount importance to find an optimal strategy to discriminate the background events. This problem can be easily faced by measuring the rate of acquired events when the radioactive source is not inserted in the chamber. So, in this case the SSB will detect spurious events due to  $\alpha$ -decay from contaminants of the chamber or from cosmic rays.

During the experimental activities, we have performed about 74 h of background acquisition, leading to the spectra of integrals and amplitudes in FIG. 11b and FIG. 11c, respectively. Through an opportune visualisation of these results, we can notice how the background events are concentrated in a region after the amplitude value of 3500 mV, which is outside of the signal region. So, the real background event rate when we select the events in the

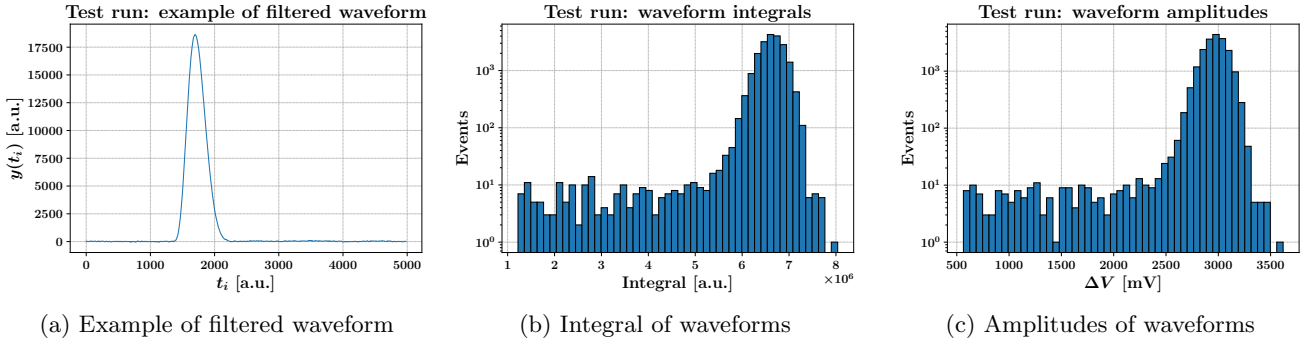


**FIG. 10** Results for the test run and workflow for acquisitions with SSB detector. The filtered waveform shape is represented in 10a, while the their integrals and amplitudes are showed in 10b and 10c, respectively.

amplitude signal region, is lower than the one found by simply dividing the total events over the 74 h of acquisition by the total acquisition time.

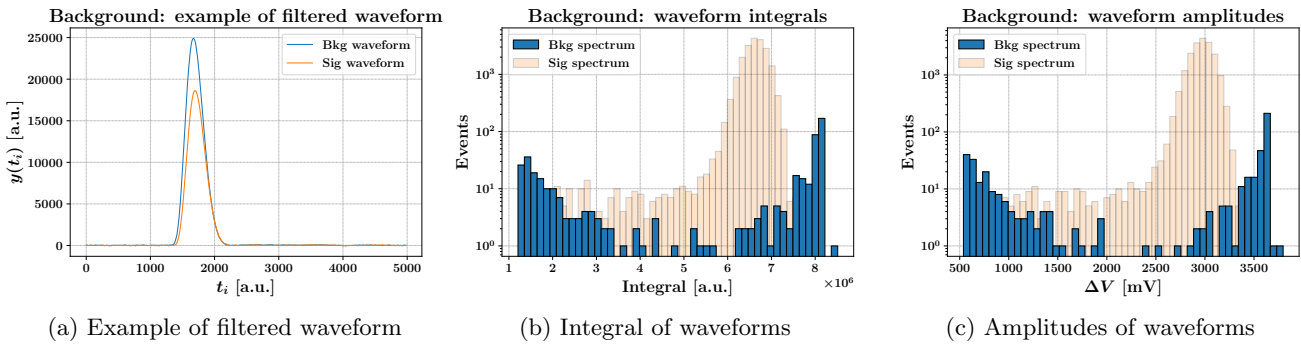


**FIG. 11** Results for the run of background acquisition. A sample filtered waveform shape is showed in 11a for both a signal and a background event. The spectra of integrals and amplitudes of all the events acquired are showed in 11b and 11c, respectively.

**c. Dead time discussion** Let us resume the discussion on the optimal choice of the number of segments in which we divide the memory of the PicoScope oscilloscope. This is an important and critical parameter when acquiring since it allows us to reduce the dead time contribution to the acquisition. Therefore, we choose a higher number of memory blocks when we expect higher rates, on the other hand we choose a lower one when we expect lower rates. However, even when an optimal choice can not be found, we can solve the problem by applying a correction on the total acquisition time. This is done by subtracting the sum of the time intervals in which the trigger is not active, but in a reset status. The ladder quantities can be retrieved from the timestamps provided by the acquisition system.

## 2. ALPIDE detector characterisation

**a. Signal integrity analysis** The connection from the FPGA to ALPIDE is made of 8 cables. Two of them are highly sensitive to external factors like noise introduced by the NIM electronics chain or the crosstalk between the cables. Some precautions are applied to reduce these effects. Each sensible cable is wrapped with a ground lead. Moreover, they are placed away from other cables that may induce noise. On the other hand, an external power supply is used to power the FPGA board instead of powering it via USB. By this way, we are able to decouple the board from the PC supply systems<sup>3</sup>.

<sup>3</sup> The various grounds (vacuum chamber, ALPIDE, SSB and PC systems) are not connected together

To verify the correct signal integrity a basic test can be used: a second FPGA (DE0-nano board equipped with a Cyclone IV by Altera [15]) has the purpose to listen only to the continuous readout command and, after receiving it, a number sequence is sent and checked via software. If the sequence does not match, it will increase a counter and at the end of the test it gives the percentage of the corrupted data.

Many cable types have been tested during the experimental activity: jumper cables, flat ribbon cables, and modified cat 7 ethernet cable. The results of the previous test with each of them are reported in TAB. V.

Cable type	Throughput <sub>theo</sub> [Mbps]	Throughput <sub>exp</sub> [Mbps]	Time [h]	Corrupted data [%]
Jumper	4.174	4.120	10	0
Flat Ribbon Cable	4.174	0	0.5	FAILED
Cat 7	4.174	4.120	10	0

TAB. V Results of the test for signal integrity with several types of cable and comparison between them.

**b. Signal-to-noise discrimination** Differently from the SSB detector, the ALPIDE detector is really sensitive to many sources of background, the main ones being cosmic rays, whose source is external to the experiment, and X-rays, produced by the radioactive source. It is therefore important to characterise the behaviour of the detector in order to discriminate these two from the  $\alpha$  particles.

The first study concerns the size and shape of the clusters generated on the detector from each type of radiation. This is accomplished by acquiring data in three different configurations of the radioactive source:

- no source in the chamber: in this case we see only cosmic rays;
- shielded source: in this case we put the radioactive source in front of the detector but we cover its face with some layers of paper in order to stop the  $\alpha$  particles contribution but not the X-rays. With this configuration, we can acquire data about the full background;
- direct radiation: this last configuration is equal to the previous one minus the paper shield. In this case we obtain a sample with all the types of radiation.

To automatically detect the traces in each situation, we employ a clustering algorithm, chosen among the possibilities of DBSCAN and Agglomerative-Clustering, offered by the Scikit-Learn Python library. A simple test to identify the best one shows how DBSCAN offers a better noise discrimination, hence it is chosen against the Agglomerative-Clustering method. Given this detail, we present some significant samples of hitmaps in FIG. 12, where the several types of source and background radiations can be observed, while the pixel noise is rejected in both of them.

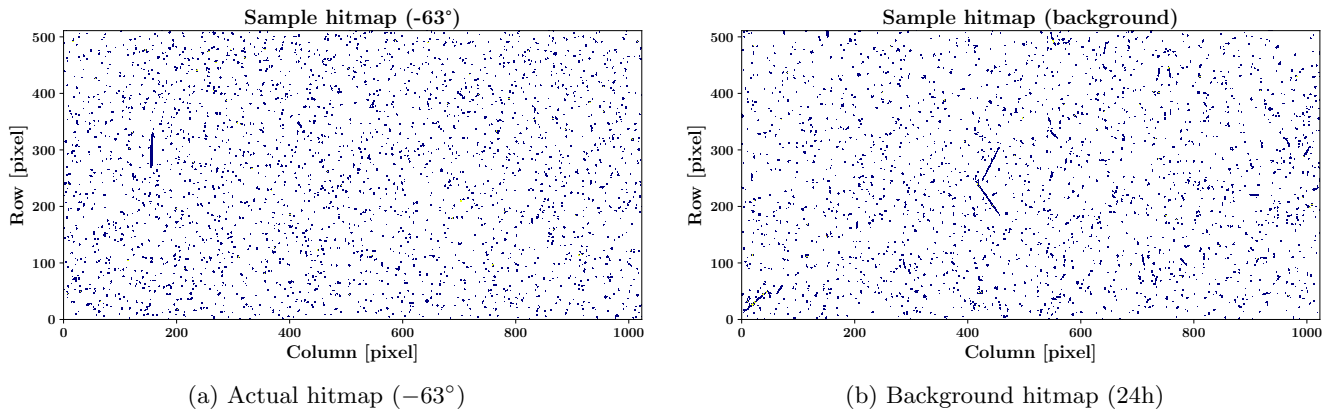
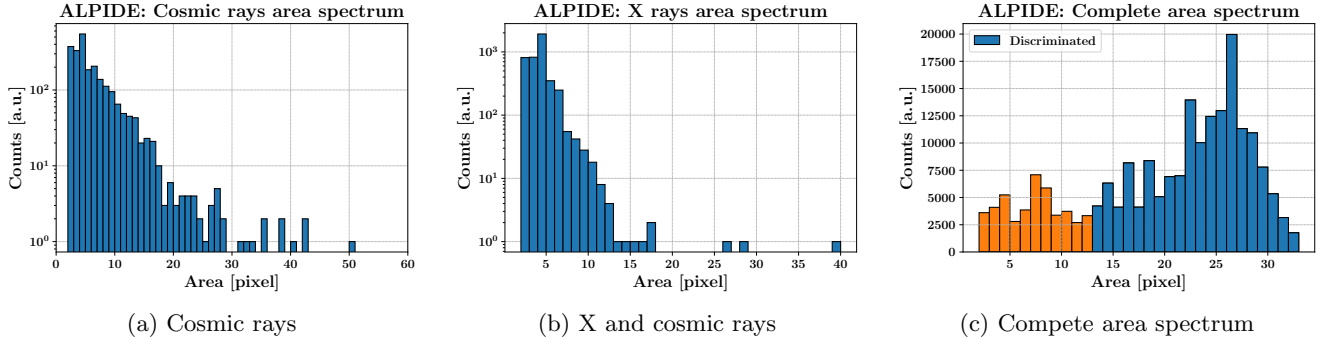


FIG. 12 Sample hitmaps of the clusters revealed by ALPIDE detector. In 12a, an example of hitmap acquired at an angular position of  $-63^\circ$  with respect to the beam direction. In 12b, an example of hitmap from background acquisitions. The longer traces come from cosmic rays, while the bigger circular clusters are due to  $\alpha$  particles. Lastly, the smaller circular clusters are due to X-rays.

The best parameters to identify the type of radiation are the size of the cluster and the ratio of the variance along the two main directions of the trace. The ladder quantity is obtained by the application of a PCA algorithm to the

cluster and finding the ratio between the variances along the main axes, namely the “PCA ratio”. The results of this analysis are showed in FIG. 13 and FIG. 14. As we can see from these plots, the  $\alpha$  particles are characterised by big clusters: their area distribution presents a clear peak around 25 pixels, and small PCA ratios ( $\sim 1.5$ ). On the other hand, cosmic rays present very high PCA ratios and a wider area spectrum. Most cosmic rays have small areas ( $\sim 6$  pixels) but, in some cases, the most energetic ones and the ones that are parallel to the detector surface are able to activate several dozens of pixels. Last but not least, the X-rays present an area distribution peaked to around 4 pixels.



**FIG. 13** Size of the cluster induced by different types of radiation on the ALPIDE detector. In 13a, the distribution for cosmic rays, while in 13b the distribution for both X and cosmic rays. Lastly, in 13c, the discriminated  $\alpha$  particles distribution in the complete area distribution.

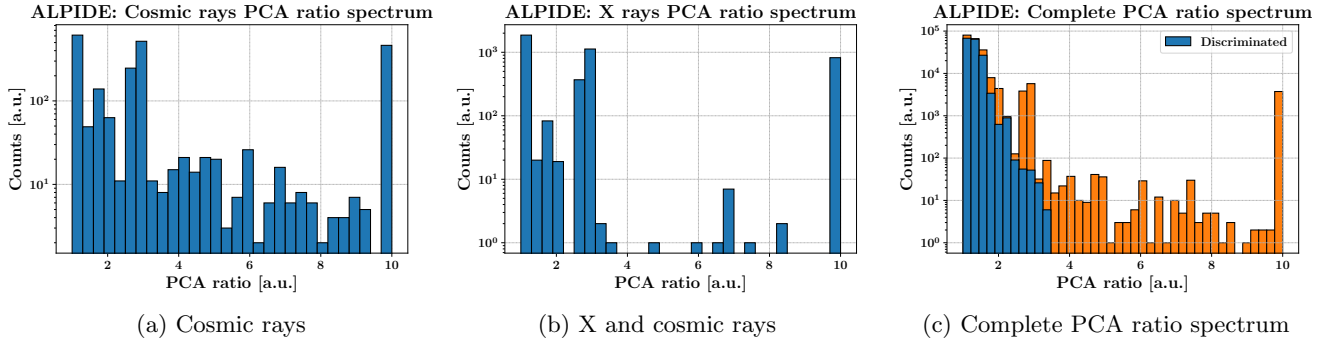


**FIG. 14** Ratio between the variance on the two main cluster components computed with a PCA algorithm for different types of radiation on the ALPIDE detector. In 14a, the PCA ratio for cosmic rays, while in 14b the PCA ratio for both X and cosmic rays. Lastly, in 14c, the discriminated  $\alpha$  particles PCA ratio in the complete distribution.

We report the mean values of the cluster area and PCA ratio for all the types of radiation in TAB. VI. Using this information, we can statistically discriminate signal events from background ones by considering only clusters with area  $A > 12$  and PCA ratio  $P_r < 3.5$ . In the same table we report also the mean values for a discriminated set of clusters, indicated with the notation  $\alpha_{\text{disc}}$ . As we can see, the mean area increases and it is very close to the peak value of 25 pixels observed in FIG. 13c.

**c. Threshold analysis** The threshold at which the pixel fires when a particle traverses is mainly set by the  $I_{\text{THR}}$  and  $V_{\text{CASN}}$  values [10]. These parameters can be modified by writing the DAC value on a given register [10], which has 8 bit resolution and sweeps from AVSS (equal to 0 V) to AVDD (equal 1.8 V)<sup>4</sup>. The charge threshold is decreased by augmenting  $V_{\text{CASN}}$  and vice versa, it is increased by increasing  $I_{\text{THR}}$ .

<sup>4</sup> Some DACs have a unitary gain buffer which introduces an offset of 370 mV;  $V_{\text{CASN}}$  is not one of them, in fact it is directly connected to the pixel matrix.

Particle	Area [pixel]	PCA ratio	Rate [ev/h]
Cosmic rays	$6.0 \pm 6.3$	$3.9 \pm 3.3$	$5.79 \cdot 10^2$
X rays	$3.8 \pm 1.6$	$3.4 \pm 3.3$	$2.88 \cdot 10^4$
$\alpha$	$19.5 \pm 8.0$	$1.6 \pm 1.2$	$1.46 \cdot 10^6$
$\alpha_{\text{disc}}$	$23.0 \pm 4.8$	$1.3 \pm 0.2$	$1.15 \cdot 10^6$

**TAB. VI** Summary of the main cluster features for different types of radiation and for a discriminated sample  $\alpha_{\text{disc}}$ .

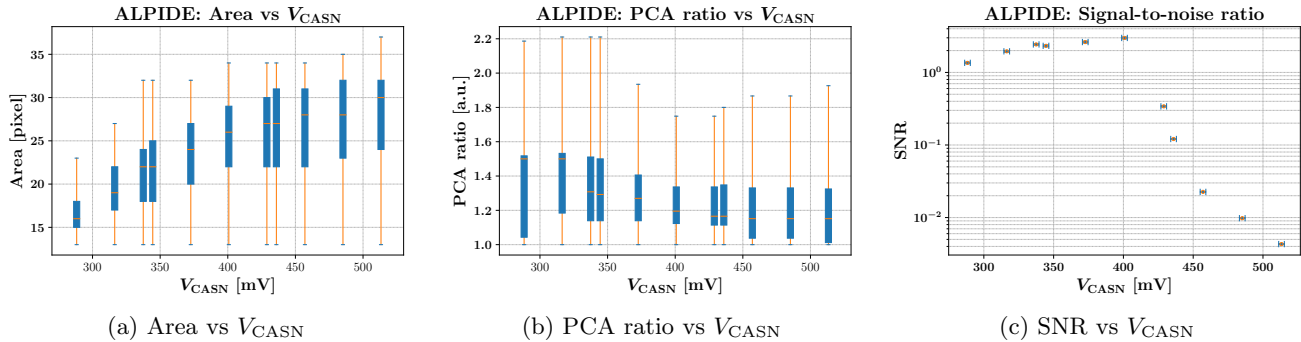


**FIG. 15** Results for  $V_{\text{CASN}}$  parameter optimisation. In particular, in **15a**, **15b** and **15c** the Area of clusters, the PCA ratio and the SNR in function of  $V_{\text{CASN}}$ , respectively.

In our studies,  $V_{\text{CASN}}$  is the only parameter modified (register 0x0604). We report in FIG. 15 the results of some tests performed to find the optimal value of  $V_{\text{CASN}}$ , in order to maximise the discrimination power of our methods to distinguish between X-rays, cosmic rays and  $\alpha$ -particles.

Firstly a simple software threshold is set to discard X-rays and eventual cosmic rays<sup>5</sup>, so that only clusters with area above 12 pixels and PCA ratio below 4 are considered. A higher value of the mean area threshold leads to a better discrimination between unwanted particles. As it showed in FIG. 15a, the dependence on  $V_{\text{CASN}}$  becomes weaker at higher values.

In FIG. 15b we highlight how the PCA ratio dispersion has a minimum around  $V_{\text{CASN}} = 400$  mV, with higher values for lower  $V_{\text{CASN}}$ . It is clear from FIG. 15c that going beyond 400 mV implies a lower SNR and considering the readout limitations introduced above, a value of 373 mV is selected (corresponding to a value of 0x0035 on the register). This value of  $V_{\text{CASN}}$  gives us the best compromise between particle discrimination and acquirable rate.

**d. Timing analysis** As we have highlighted in the previous discussion, due to the limitations introduced by the slow port, it necessary to make some compromises on the readout speed. This is accomplished by tuning the time fraction in which the detector can store the data, namely the so-called **STROBE**, and the gap between two subsequent trigger signals, namely the so-called **GAP**, both expressed in units of clock cycles. We observe that if the strobe time is too low, the charge produced by the  $\alpha$  particles can not be completely collected and therefore the discrimination from the X-rays is problematic. So, a value of 5000 clock cycles is selected<sup>6</sup> to avoid this drawback.

To avoid the FIFO overflow, the gap needs to be tuned for each case. For small angles where the expected rate is higher, a larger gap value is set, while for higher angles a lower gap is selected due to the lower statistics. The effective exposition time  $t_{\text{exp}}$  of ALPIDE will follow the expression:

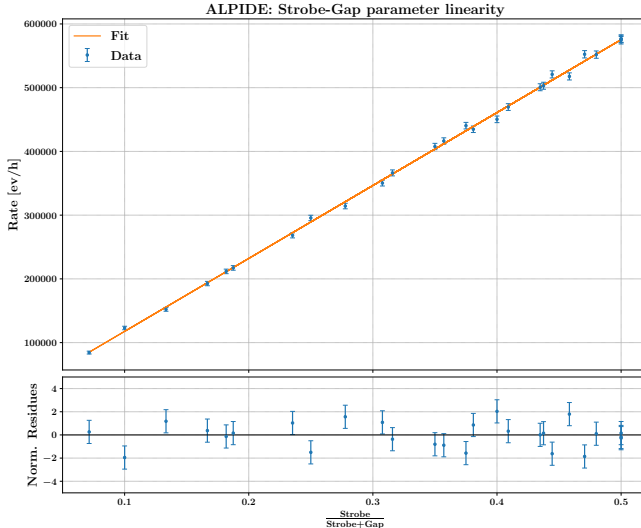
$$t_{\text{exp}} = t_{\text{acq}} r = t_{\text{acq}} \frac{t_{\text{strobe}}}{t_{\text{strobe}} + t_{\text{gap}}} . \quad (14)$$

A test to verify the linearity of the effective exposition time in EQ. 14 can be performed. With this purpose, the radioactive source is placed at a fixed distance from ALPIDE and an acquisition is launched for different values of strobe and gap, with an acquisition time of 60 s, and then measuring the rate. A plot with the results of this study

<sup>5</sup> This software threshold is tuned once the optimal  $V_{\text{CASN}}$  is chosen.

<sup>6</sup> Corresponding to 125  $\mu$ s

is showed in FIG. 16, where we perform also a linear fit to verify the linear trend of the rate with respect to the ratio  $r$  of strobe and strobe plus gap.



(a) Plot of measurements, fit and residuals

Data					
Strobe cycles	Gap cycles	Rate [10 <sup>3</sup> . ev/h]	Strobe cycles	Gap cycles	Rate [10 <sup>3</sup> . ev/h]
20000	45000	350 ± 5	35000	45000	503 ± 5
45000	45000	574 ± 6	30000	45000	450 ± 5
30000	65000	366 ± 5	50000	65000	501 ± 5
60000	65000	552 ± 6	25000	25000	577 ± 6
40000	65000	435 ± 5	25000	65000	314 ± 4
20000	25000	521 ± 6	45000	65000	470 ± 5
35000	65000	408 ± 5	10000	45000	212 ± 3
55000	65000	518 ± 6	40000	45000	552 ± 6
15000	45000	296 ± 4	20000	65000	268 ± 4
25000	45000	416 ± 5	15000	25000	440 ± 5
15000	65000	217 ± 4	10000	65000	152 ± 3
5000	65000	84 ± 2	5000	45000	123 ± 3
65000	65000	576 ± 6	5000	25000	192 ± 3

Fit Results			
m [10 <sup>3</sup> . ev/h]	q [10 <sup>3</sup> . ev/h]	$\chi^2$	d.o.f.
1144 ± 7	3 ± 2	31	24

(b) Measurements and fit results

**FIG. 16** Measurements of the acquired rate of events with different values of strobe and gap, which are given in units of clock cycles. In FIG. 16a, the rate is plotted in function of the ratio of the strobe and strobe plus gap, namely  $r$ , alongside with the linear fit performed and the normalised residuals. In TAB. 16b, the acquired data and the results of the linear fit are reported.

From the fit results, we observe how our data are compatible with a linear trend and so we can extrapolate useful information for the setup optimal working point:

- the effective rate that we expect at zero angular position is the slope value  $m$  of the linear fit;
- the intercept value  $q$  is in good compatibility with the expected value of 0, which means that our measurements are not affected in a relevant way by systematic uncertainties;
- furthermore, both PCA ratio and cluster area do not show any dependence on the selected strobe-gap parameters.

### 3. Radioactive source characterisation

**a.  $\alpha$  exit energy** Focusing on the  $\alpha$  emissions of the source, we have previously listed the main decay product energies in TAB. IV. However, when detecting these particles, we will not find these exact energies. In fact, the active material of  $^{241}\text{Am}$  is followed by multiple gold plates, which cause a partial loss of energy due to **straggling** effects. Dealing with this phenomenon is simple, but at the same time accurate, by following the same approach in [16]. We model the energy loss with a Gaussian distribution  $f(\mathcal{E}_{\text{loss}}) = G(\mu, \sigma)$ , whose parameters are:

$$\begin{aligned} \mu &= S(\mathcal{E}_\alpha) \rho \Delta x \\ \sigma^2 &= 4\pi \left( \frac{e^2}{4\pi\varepsilon_0} \right)^2 z_\alpha^2 Z N \Delta x \end{aligned} \quad , \quad (15)$$

where:

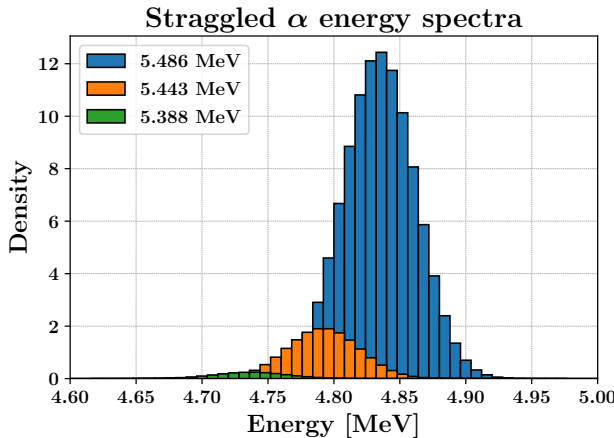
- $S(\mathcal{E}_\alpha)$  is the material stopping power at  $\mathcal{E}_\alpha$  energy;
- $z_\alpha$  and  $Z$  are the  $\alpha$  particle and the target atomic numbers, respectively;
- $N$  is the number of atoms per unit of volume;
- $\Delta x$  and  $\rho$  the gold plates total thickness (in cm) and density (in g/cm<sup>3</sup>), respectively.

The beam distribution will be the convolution of three delta distributions (one for each decay channel), convolved with the corresponding energy loss distribution. Therefore, the spectrum of  $\alpha$  particles after traversing the gold plates can be modelled with the sum of three Gaussians<sup>7</sup>:

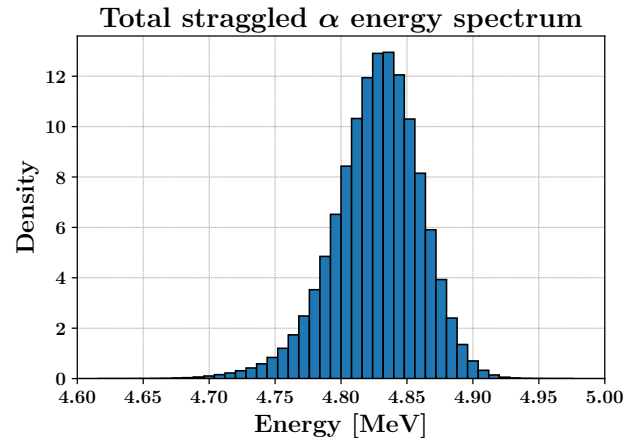
$$f(\mathcal{E}_{\text{beam}}) = \sum_i f_i G(\mathcal{E}_i - \mathcal{E}_{\text{loss},i}, \sigma_i) , \quad (17)$$

where  $f_i$  is the decay fraction of the  $i^{\text{th}}$  channel and  $\mathcal{E}_i$ ,  $\mathcal{E}_{\text{loss},i}$  and  $\sigma_i$  are the  $\alpha$  energy, energy loss and standard deviation in that specific channel, respectively. The contributions from all the relevant  $\alpha$  decay channels are showed in FIG. 17a, while the shape of the total estimated distribution is showed in FIG. 17b. In particular, we find as peak energy:

$$\mu_{\text{peak}} = 4.827 \text{ MeV} . \quad (18)$$



(a) Straggled  $\alpha$  spectra for each decay channel



(b) Straggled  $\alpha$  total spectrum

**FIG. 17** Estimated energy spectrum for the  $^{241}\text{Am}$  radioactive source after the passage from a gold plate of  $1.51 \mu\text{m}$ . In 17a, all the relevant contributions to the energy spectrum; in 17b, the total energy spectrum density.

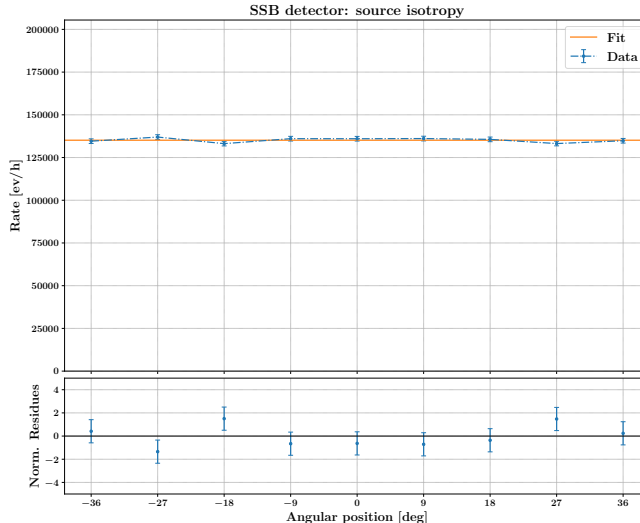
**b. Source isotropy** On the experimental side, after the calculations in the previous Paragraph on the energy loss of  $\alpha$  particles, we study the source isotropy of emission. This can be accomplished by placing the active material section of the source cylinder in the rotation axis of the support over the step motor. By this way, without collimating the beam, the SSB detector “sees” the source emissions also at large angles. Therefore, we can test if the rate of events is approximately the same in a certain angular range by fitting with  $y = w$ . The results of this test are showed in FIG. 18. As we can observe, the hypothesis of emission isotropy is reasonable, confirmed by the  $\chi^2$  over the degrees of freedom which is approximately 1.

**c. Source emissions energy-angle correlation** The last study of source characterisation concerns the  $\alpha$  particle energy correlation with the angular direction of emission. Let us consider the same configuration employed in the previous Paragraph, so the source point of emission in the centre of rotation of the motor. In principle, an  $\alpha$  particle emitted at a larger angle with respect to zero is affected by larger straggling effects, since it goes through a longer thickness of gold plate. So, we expect to observe a spectrum peak energy lower for greater angles and higher for angles near to the zero.

Before performing this study on the same dataset employed for the study of source isotropy, we define an energy calibration strategy for the energy spectrum. In the previous discussion, it has been expressed in arbitrary units. However, now that we know the central angle energy spectrum and so its peak in MeV from previous calculations, we can use this information to solve this problem. In fact:

<sup>7</sup> The convolution of a gaussian and a delta distribution can be computed as the convolution between two Gaussians, which is known to be a Gaussian distribution:

$$G_1(\mu_1, \sigma_1) \otimes G_2(\mu_2, \sigma_2) = G\left(\mu_1 + \mu_2, \sqrt{\sigma_1^2 + \sigma_2^2}\right) \Rightarrow G_1(\mu_1, \sigma_1) \otimes \delta(x - \mu_2) = G_1(\mu_1, \sigma_1) \otimes G_2(\mu_2, 0) = G(\mu_1 + \mu_2, \sigma_1) \quad (16)$$



(a) Plot of measurements, fit and residuals

Data		
Angle [deg]	Exp. time [s]	Rate [ $10^5 \cdot \text{ev/h}$ ]
-36.0	268.5	$1.346 \pm 0.001$
-27.0	262.8	$1.370 \pm 0.001$
-18.0	270.4	$1.331 \pm 0.001$
-9.0	264.6	$1.360 \pm 0.001$
0.0	264.7	$1.360 \pm 0.001$
9.0	264.5	$1.361 \pm 0.001$
18.0	265.4	$1.356 \pm 0.001$
27.0	270.3	$1.332 \pm 0.001$
36.0	267.0	$1.348 \pm 0.001$

Fit results	
$w$ [ $10^5 \cdot \text{ev/h}$ ]	$1.3514 \pm 0.0005$
$\chi^2$	7.94
d.o.f.	8

(b) Measurements and fit results

**FIG. 18** Measurements with emission point approximately in the axis of rotation and at different angular positions. In 18a, the average weighted on the inverse squared of errors is reported as a straight line and the related residues are showed in the bottom panel. In 18b, we report all the experimental measurements obtained to reproduce the plot, along with the fit results.

- we set as zero of the energy in MeV the zero of the energy in arbitrary units;
- we set the peak energy in arbitrary units for the spectrum at zero position to the value in EQ. 18.

By this way, we can extrapolate a calibration line from the data acquired at zero angular position and use it to calibrate the energy spectra for the other positions. The next operation is to take the peak energy in MeV for each case and check if it decreases for wider angles. The results for this study are showed in FIG. 19, where we model the trend of data by fitting with the following function:

$$y(\theta) = a + \frac{b}{\cos(\theta - c)} , \quad (19)$$

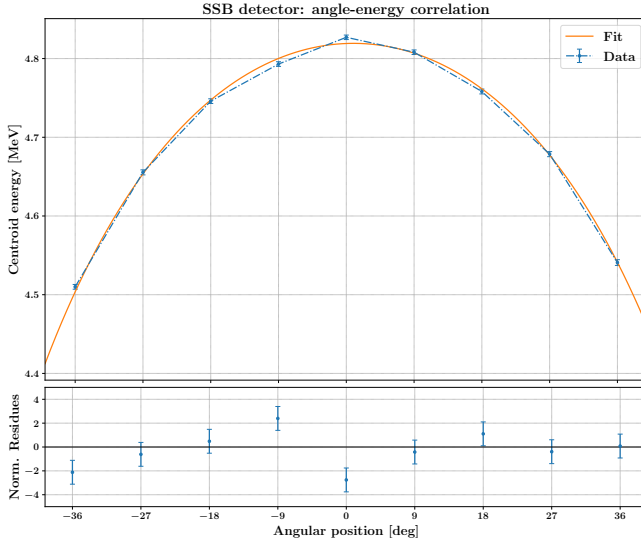
which represents the theoretical expectation due to geometrical and trigonometric considerations.

Now, if we consider the working point of a collimated beam, namely a beam concentrated in the angular region  $[-10, 10]$  degrees, we observe that the energy variation in function of the angle is a secondary effect. In fact, we would have an energy variation of about one hundred of keVs around the maximum peak energy in EQ. 18.

#### 4. Simulation of the apparatus

After having discussed all the needed characterisations of the apparatus components, we pass to the simulation of the experiment in order to model the behaviour of the apparatus itself. In particular, we simulate both the conditions of scattering foil removed or inserted, so that we can obtain a model of both the beam and scattering profiles. Moreover, we can repeat this simulation for a different foil material by simply changing its intrinsic parameters, such as its atomic number and density.

Before going on, we remark that the physics of scattering is based on the differential cross section expression in EQ. 1. In addition, we improve the model by introducing geometrical, trigonometric and physical factors, such as beam angular spread, the dimensions of the collimators of the beam and of the detectors, and the source products energy spread. The last remark to do is that the system of reference chosen has its origin in the centre of the vacuum chamber, the  $z$ -axis parallel to the beam direction and the  $y$ -axis pointing upward perpendicularly to the vacuum chamber surface. In order to fit the simulation to our setup, the positions of all the setup components are set to the values listed in the previous sections.



(a) Plot of measurements, fit and residuals

Data			
Angle [deg]	Exp. time [s]	$\mu(\theta)$ [MeV]	
-36.0	268.5	$4.510 \pm 0.003$	
-27.0	262.8	$4.655 \pm 0.003$	
-18.0	270.4	$4.746 \pm 0.003$	
-9.0	264.6	$4.793 \pm 0.003$	
0.0	264.7	$4.827 \pm 0.003$	
9.0	264.5	$4.808 \pm 0.003$	
18.0	265.4	$4.758 \pm 0.003$	
27.0	270.3	$4.679 \pm 0.003$	
36.0	267.0	$4.541 \pm 0.004$	

Fit results	
$a$ [MeV]	$6.08 \pm 0.03$
$b$ [MeV]	$-1.26 \pm 0.03$
$c$ [rad]	$0.017 \pm 0.004$
$\chi^2$	20.0
d.o.f.	6

(b) Measurements and fit results

**FIG. 19** Measurements with emission point approximately in the axis of rotation and at different angular positions. In 19a, the centroid energy in function of the angular position is plotted and fitted with EQ. 19, with the residuals in the bottom panel. In 19b, we report all the experimental measurements obtained to reproduce the plot, along with the fit results.

**a. Particle generation** Given the source surface centre  $x_{s,0}$  and its radius  $r_s = 0.335$  mm, a specified number of particles is generated with energy  $\mathcal{E}_\alpha$  taken from the distribution in FIG. 17b. Then, each particle is associated to a position  $(x_i, y_i, z_i)$ , uniformly generated inside the source surface, and to a momentum, randomly generated in the forward hemisphere with kinematics coherent with the sampled energy.

**b. Beam collimation** After the generation on the source surface, the kinematic evolution of each particle is analytically computed up to the plane of the first beam collimator. Denoting by  $w$  and  $h$  the height and width, respectively, of the collimator, the following conditions are imposed in order to further evolve the path of a particle:

$$\begin{cases} |x_i - x_{C1}| \leq \frac{w}{2} \\ |y_i - y_{C1}| \leq \frac{h}{2} \end{cases}, \quad (20)$$

where  $x_{C1}$  and  $y_{C1}$  are the abscissa and the ordinate of the first collimator, respectively. The particles not satisfying both the conditions are discarded and the same procedure is applied again after the spatial evolution to the plane of the second collimator. The particles exiting from the ladder are kept.

**c. Target scattering** The interaction with the gold foil is composed of the following passages:

- for each particle an impact parameter  $b$  is randomly generated between 0 and the mean inter-atomic distance between the atoms;
- then, the scattering angle is computed in the intrinsic frame of the particle. With respect to this frame, the azimuth angle  $\alpha$  is randomly generated in  $[0, 2\pi]$ , while the polar angle is computed from the impact parameter as:

$$\theta = \pi - 2 \cos^{-1} \left[ \frac{\frac{k}{2\mathcal{E}_\alpha b}}{\sqrt{1 + \left( \frac{k}{2\mathcal{E}_\alpha b} \right)^2}} \right] \quad \text{with} \quad k = \frac{q_\alpha Z}{4\pi\varepsilon_0}, \quad (21)$$

where  $q_\alpha$  is the charge of the  $\alpha$  particle and  $Z$  the atomic number of the target.

- each particle momentum is rotated from the intrinsic frame to the laboratory frame by an opportune combination of rotation matrices, obtained from the scattering angles.

In the implementation of the computations described earlier, the following corrections are also included in order to improve the accuracy of simulation of the intrinsic physics:

- atomic charge screening: the effective charge seen by the particle is not equal to  $Ze$ , but it depends on the impact parameter. This effect is modelled by a (descending) exponential distribution, whose maximum is equal to  $Z$  for  $b = 0$  nm and it saturates at a characteristic value  $Z'$  at the atomic radius  $r_a$ ;
- energy loss due to straggling with foil: each particle energy and momentum is reduced according to the energy loss of a charge carrier when traversing a foil of a certain material.

**d. Detector acquisition** Similarly to what has been already done for the collimators, the detection of the scattered particles is implemented by spatially evolve them up to a distance from the centre of rotation of the motor equal to distance from the detectors, given in TAB. II. In particular, for the specific case of SSB and ALPIDE detectors, the particles are respectively required to satisfy:

$$\begin{aligned} |y_i - y_{CD}| &\leq \frac{r_p}{2} \\ |y_i - y_{CD}| &\leq \frac{h}{2} \end{aligned}, \quad (22)$$

with  $r_p$  being the radius of the collimator of SSB detector and  $h$  the height of ALPIDE detector matrix. Lastly, the particles that are not discarded are the ones detected. Thus, from their final position it is possible to extract their angular position and, then, to compute the final angular distribution, taking as reference the centre of rotation of the motor and of the vacuum chamber.

## 5. Characterisation of beam profile and validation of simulation

In order to validate the simulation implementation and its results, we take as benchmark the beam profile of the radioactive source, namely the final angular distribution measured without the scattering foil. On the simulation side, we replicate this setup by not inserting the scattering foil in the apparatus simulated components. The comparison between the simulated and the experimental angular distributions of the beam is showed in FIG. 20a and FIG. 20b, respectively for SSB and ALPIDE detectors. It is possible to observe how the simulation replicates the trend of the experimental angular distribution, validating the implementation of the model.

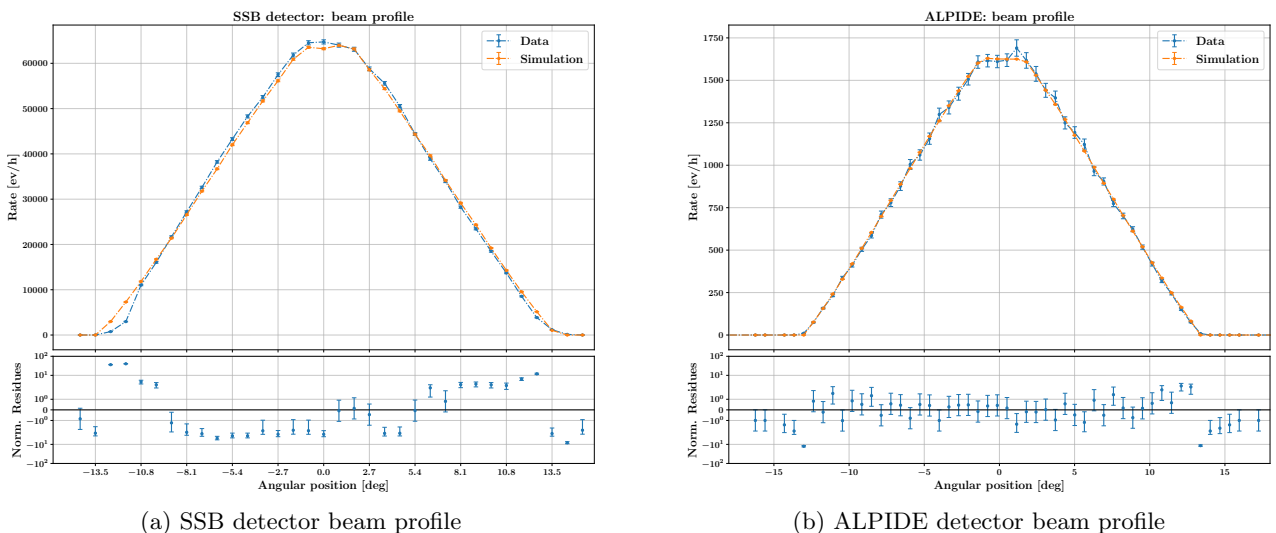


**FIG. 20** Beam profile comparison between the numerical simulation and the acquired spectrum with the SSB detector in FIG. 20a and with the ALPIDE detector in FIG. 20b.

## IV. EXPERIMENTAL DATA ANALYSIS AND RESULTS

After having performed all the tests for the setup characterisation, we discuss in this Section the technical details of the final measurements for the scattering process and then we treat the analysis of the acquired data. Lastly, we present the methods employed to extract meaningful results from the measurements and, to conclude, we discuss their significance.

### 1. Data acquisition planning

Using the information provided by the numerical simulation of the scattering process, we have planned a series of acquisitions of different duration, depending on the angular position of the detector with respect to the beam centre. Aside from the time extension of the acquisitions, there are other parameters to take into account for a correct execution of this part of experiment. In particular, for every angle:

- we should set a reasonable number of memory blocks for the SSB acquisition system, in order to make the dead time correction negligible;
- we must choose an optimal configuration of strobe and gap values for the ALPIDE detector, in order to avoid the overflow of the FIFO pipeline and the consequent corruption of the acquired data.

More precisely, for the SSB detector we identify five regions and for each of these we establish an angular interval of acquisition and the number memory blocks to use. On the other hand, for ALPIDE detector, due to its wider angular opening, we acquire at regular intervals, selecting each time the correct combination of the aforementioned parameters. A brief summary of the position, duration and parameters of the acquisitions is reported in TAB. VII and TAB. VIII for both SSB and ALPIDE detection systems.

SSB detector				
Angle [deg]	Sampling interval [deg]	Samples per block	Programmed	$t_{\text{acq}}$ [h]
$ \theta  \in [0.0, 9.0[$	2	100	1	
$ \theta  \in [9.0, 18.0[$	2	10	4	
$ \theta  \in [18.0, 27.0[$	2	1	8	
$ \theta  \in [27.0, 36.0[$	5	1	24	
$ \theta  \in [36.0, 54.0[$	10	1	72	

**TAB. VII** Programmed acquisition times for each angular region for SSB detection system, along with the corresponding chosen number of memory blocks for dead time reduction.

ALPIDE detector				
Angle [deg]	Strobe [ $10^3$ clk cycles]	Gap [ $10^3$ clk cycles]	Programmed	$t_{\text{acq}}$ [h]
$\pm 0$	5	65	1	
$\pm 9.0$	5	65	2	
$\pm 18.0$	5	45	4	
$\pm 27.0$	5	25	12	
$\pm 36.0$	5	25	24	
$\pm 45.0$	5	25	48	
$\pm 54.0$	5	15	72	
$\pm 63.0$	10	15	72	

**TAB. VIII** Programmed acquisition times for each angular position for ALPIDE detection system, along with the corresponding chosen values for strobe and gap parameters.

## 2. Scattering angular distribution

As pointed out in the previous Section, strobe and gap parameters must be tuned for each expected rate. This configuration translates into the fact that some angle fractions are exposed multiple times with different parameters. Therefore, to compute the total rate it is necessary to firstly estimate the exposure time for each angle. Considering ALPIDE active matrix centred at a specific angular position and taking into account all the data acquisition runs, a histogram of the total exposure time can be constructed. For instance, we show it for the case of gold scattering data in FIG. 21a, while we prove the usefulness of the ladder by showing the raw acquired events without time normalisation in FIG. 21b. In particular, the normalisation is applied by dividing the total raw events distribution by the histogram of total exposition time.

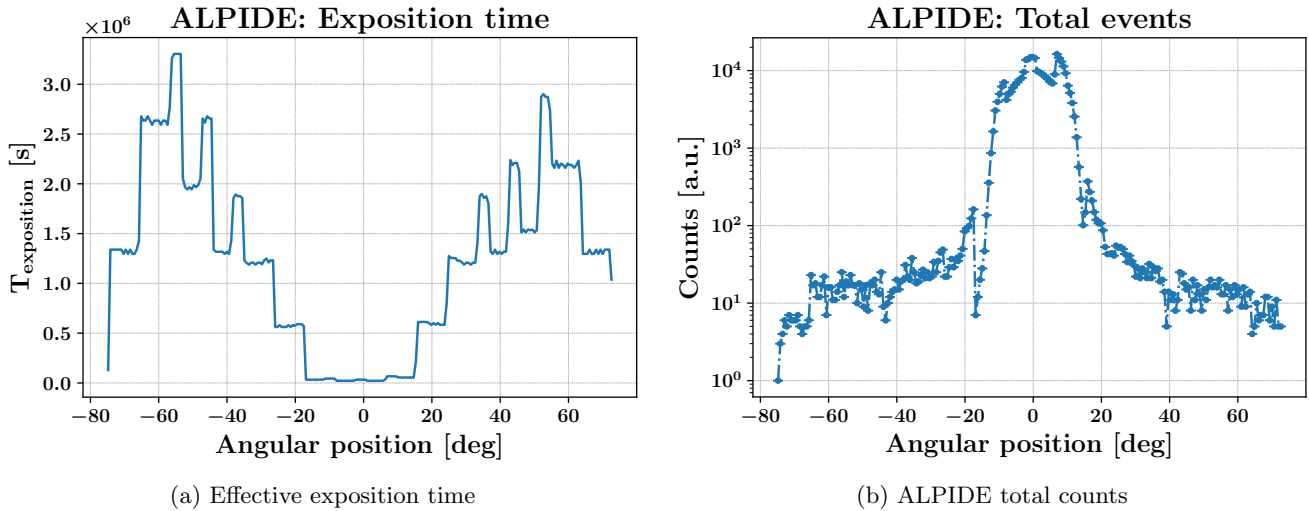


**FIG. 21** ALPIDE rate normalisation on effective exposition time. In 21a, the histogram of the total exposition time for the gold foil data, used as normalisation of the total angular distribution in 21b.

The same procedure is not applied in the SSB system analysis, because of the small solid angle covered by the collimated silicon detector. In fact, the rate is evaluated for a discrete set of angles. For this reasons, we can not directly compare the rates obtained with the two detectors, but we will treat them independently. Hence, we present in FIG. 22 and FIG. 23 the final scattering distribution acquired by SSB and ALPIDE detectors, respectively, and for the gold foil. On the other hand, we present in FIG. 24 and FIG. 25 the final scattering distribution for both the detectors and for the tin foil. We remark how the results with ALPIDE have a finer angular resolution even with lower acquisition times. This behaviour is due to the intrinsic properties of ALPIDE and to its higher acceptance with respect to the SSB detector. On the other hand, the SSB system offers an easier treatment of signal and background events, since it allows to sample the waveforms for each event registered.

## 3. Statistical analysis

**a. Gold foil analysis** Let us focus on the results for the gold foil. We immediately observe that the tails of the distributions showed in FIG. 22 and FIG. 23 are populated with respect to the case of the beam profile. This is a clear evidence of the fact that the  $\alpha$  particles undergo to Rutherford scattering when traversing the scattering foil. Here, we try to give statistical significance to this evidence.

In order to compare the theoretical distribution, provided by the simulation, with our experimental results, we employ two statistical tests. The first one is a standard  $\chi^2$  estimator, computed as the square sum of the normalised residuals, while the second one is the Two-Sample Kolmogorov–Smirnov (KS) test. Due to the significant variation in the order of magnitude of the rate along the scattering profile, it is convenient and more reliable to conduct the tests only for the tails of the distributions, namely the angular regions with  $\theta \leq -30^\circ$  (left tail) and  $\theta \geq 30^\circ$  (right tail). The results of the tests are reported in TAB. IX.

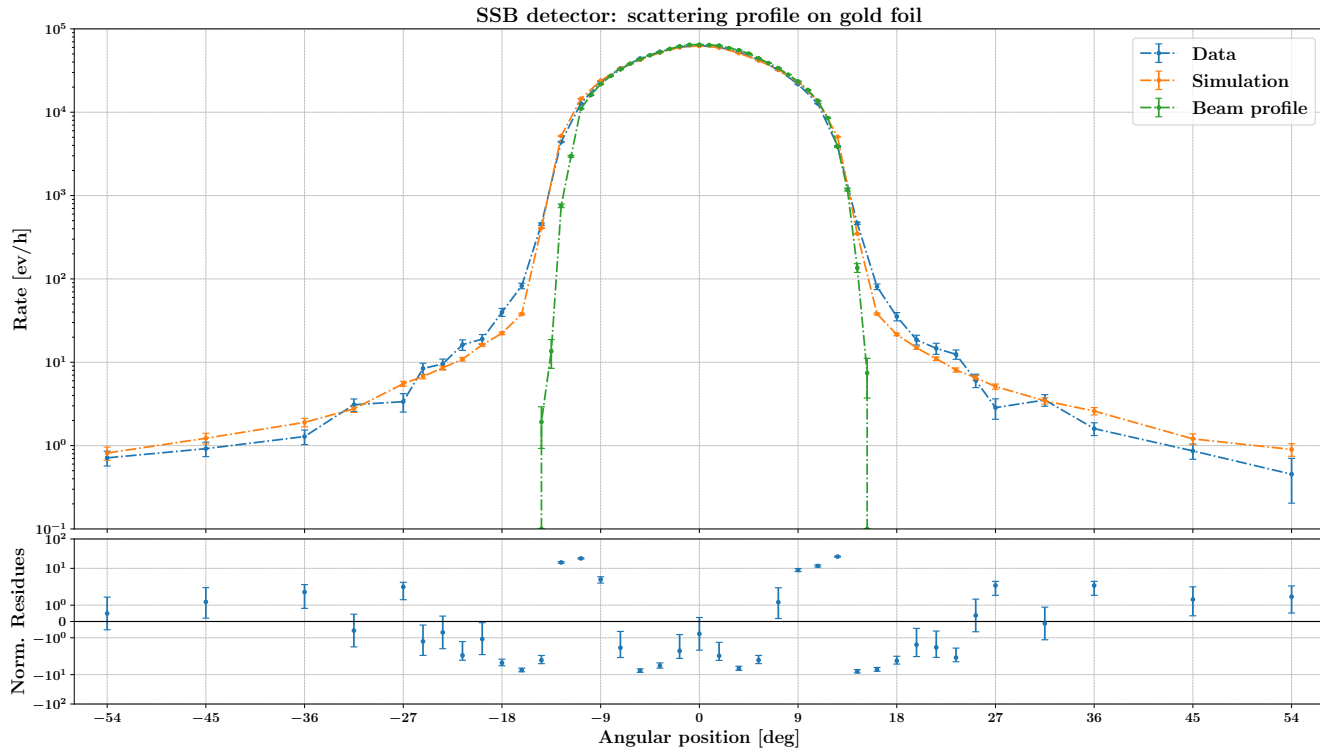


**FIG. 22** Scattering angular distribution extracted from SSB system data and for a gold foil as target.

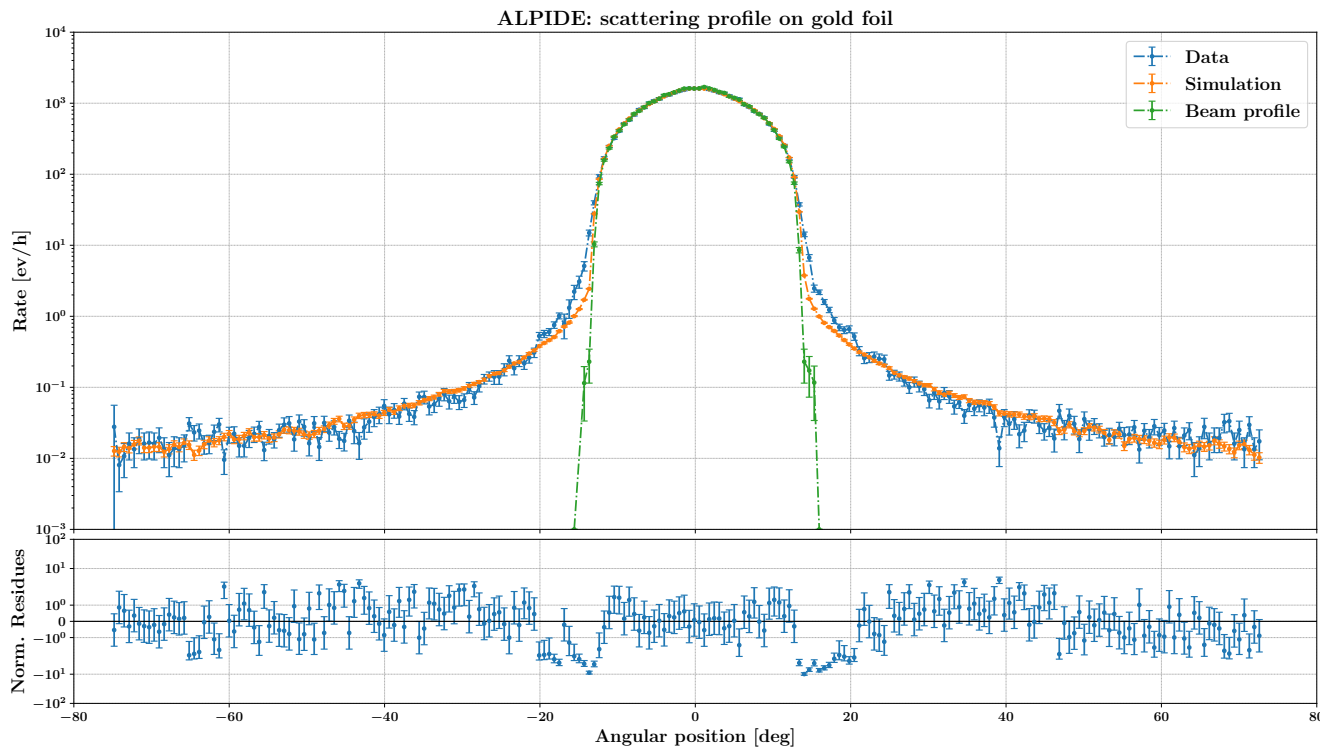


**FIG. 23** Scattering angular distribution extracted from ALPIDE system data and for a gold foil as target.

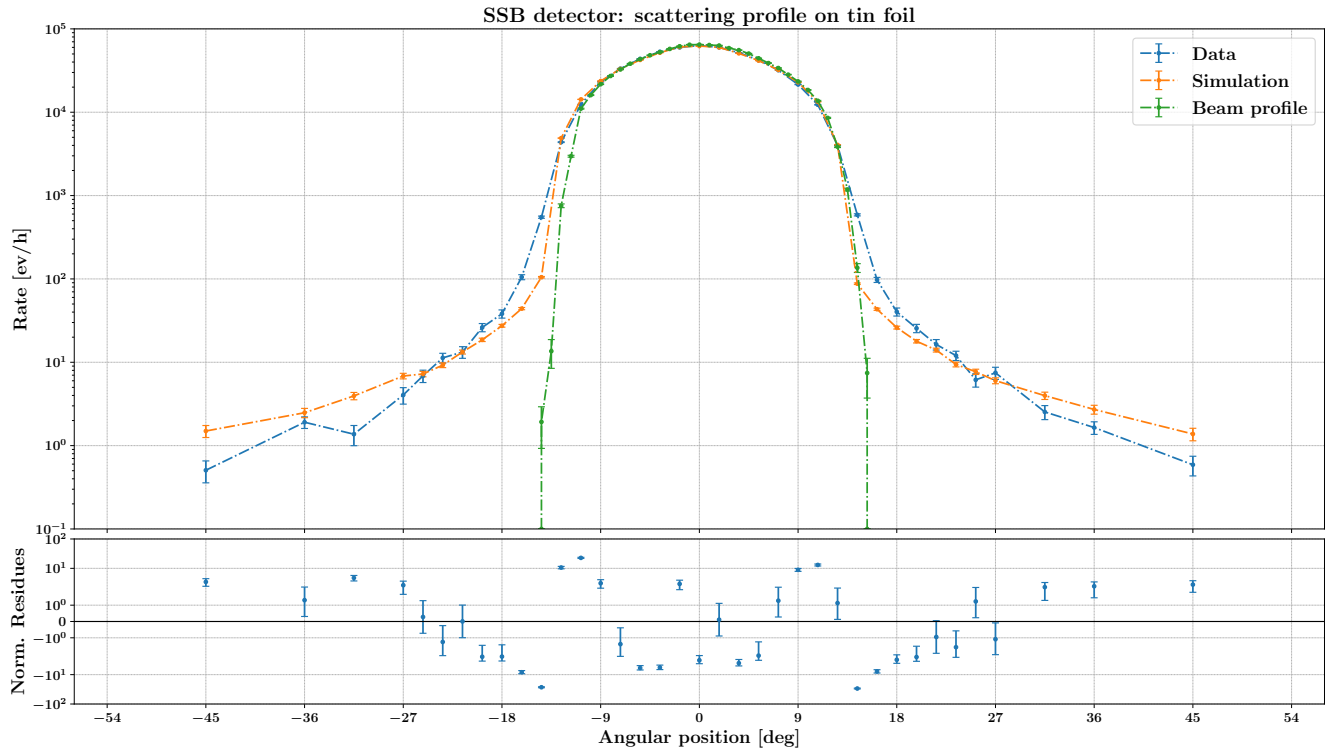


**FIG. 24** Scattering angular distribution extracted from SSB system data and for a tin foil as target.

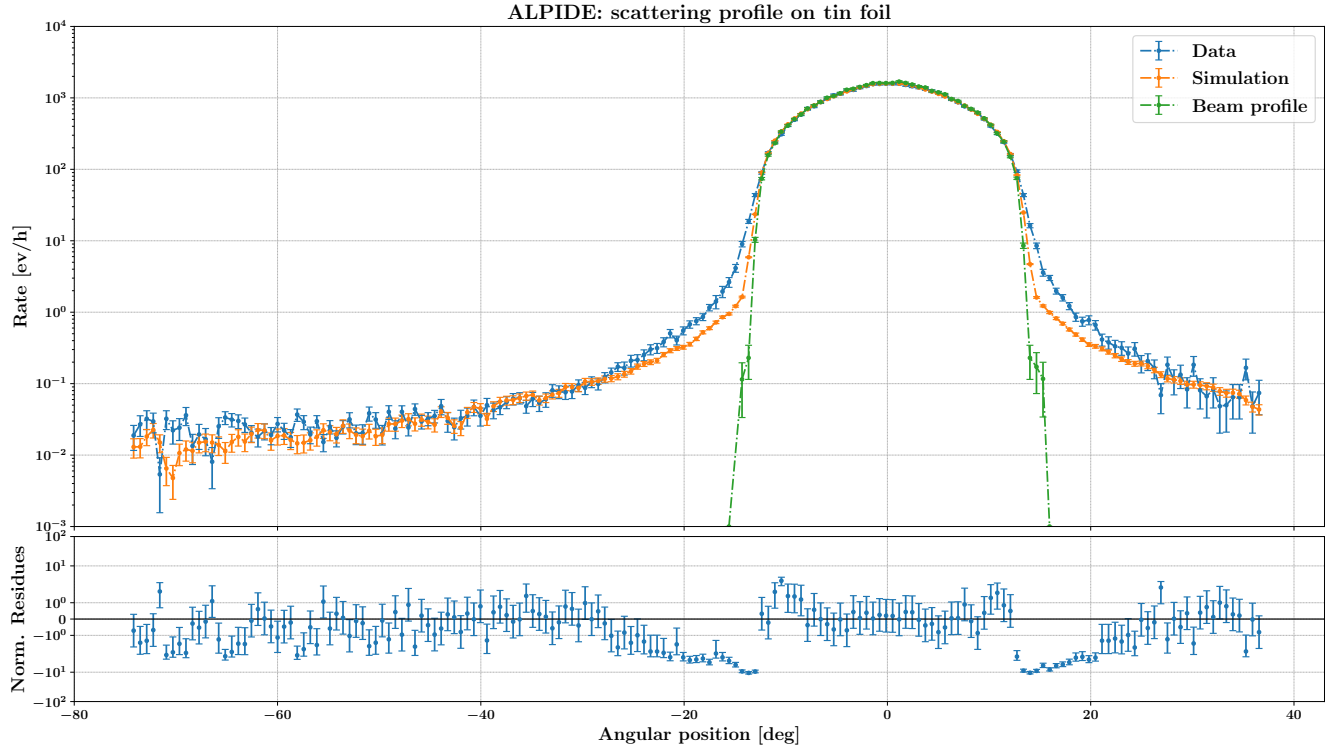


**FIG. 25** Scattering angular distribution extracted from ALPIDE system data and for a tin foil as target.

Distribution	$\chi^2$ test		KS test		
Detector Interval	$\chi^2$	n.d.f.	$\alpha$	$D^{\text{crit}}$	$D_{n,m}$
ALPIDE	$\theta < -30^\circ$	72	75	0.05	0.059 0.055
	$\theta > +30^\circ$	83	71	0.05	0.062 0.067
SSB	$\theta < -30^\circ$	5.2	4	0.05	0.14 0.09
	$\theta > +30^\circ$	11	4	0.05	0.14 0.21

**TAB. IX** Results for  $\chi^2$  and KS tests applied to the data in the tails of the scattering distributions, acquired with SSB and ALPIDE detectors with gold foil.

**b. Tin foil analysis** We repeat the same analysis and we apply the same tests to the data acquired with the tin foil. Also in this case we can observe that the tails of the distributions in FIG. 24 and FIG. 25 are populated with respect to the case of the beam profile. However, due to time limitations, we could acquire only the left tail with ALPIDE detector. As for the previous case, we run a Monte Carlo simulation of the experiment as a theoretical reference for our experimental results. The results for the  $\chi^2$  and the KS tests are reported in TAB. X.

Distribution	$\chi^2$ test		KS test		
Detector Interval	$\chi^2$	n.d.f.	$\alpha$	$D^{\text{crit}}$	$D_{n,m}$
ALPIDE	$\theta < -30^\circ$	87	75	0.05	0.061 0.058
	$\theta > +30^\circ$	***	***	***	***
SSB	$\theta < -30^\circ$	7.9	3	0.05	0.17 0.21
	$\theta > +30^\circ$	4.2	3	0.05	0.17 0.16

**TAB. X** Results for  $\chi^2$  and KS tests applied to the data in the tails of the scattering distributions, acquired with SSB and ALPIDE detectors with tin foil.

#### 4. Discussion of results

As it is possible to observe from all the scattering distributions, there is a always a small deviation of experimental data from the simulated distribution around the region of  $\sim |\theta| = 20^\circ$ . Let us focus on the physical motivation of this phenomenon. What happens in a real experiment is that some  $\alpha$  particles arriving at the border of the final second collimator of the beam are not stopped, but only braked, and so they continue to travel to the detector. In the simulation we do not consider this behaviour since for the final analysis we are interested only in the tail regions, namely to  $|\theta| \geq 30^\circ$ . Another factor not considered in the simulation is the multiple scattering, but this is a second order effect for this type of analysis, so we ignore it.

We return now to the final analysis and to the results of the statistical tests. Focusing on the gold foil dataset, we observe from TAB. IX that there is a good agreement between the expected results and the acquired ones for both the tails for ALPIDE detector and only for the left tail for SSB detector. On the other hand, for the tin foil dataset, we find a good agreement only for ALPIDE on the left tail, while for the other cases we find some discrepancies.

For both the foils, the deviations from the expected distribution may be caused by the low statistics acquired by the SSB detector, affected by a very low acceptance value. On the other hand, the simulation should be improved in order to take into account more realistically the microscopic structure of the foil, for example by including the metal structure. Another factor that may influence the statistical results is the eventuality of an imperfect alignment of the detectors in the transverse direction with respect to the beam. Further analysis in this sense should be done in the future iterations of the experiment. Last but not least, higher statistics of acquisition should be chosen in order to smooth the angular distributions and reduce the statistical fluctuations. This was not possible during this year iteration due to the limited amount of time at our disposal.

## V. CONCLUSIONS

**a. Summary** In this work we discuss the construction of an experimental setup to study Rutherford scattering interactions of  $\alpha$  particles on different target foils. The setup is composed of a vacuum chamber inside of which we position a radioactive source on top of a motorised support. The ladder allows us to rotate the source, and consequently the beam direction, making possible to acquire in a wide range of angles.

Inside the chamber two detectors are positioned at a fixed distance from the axis of the motor, in order to reveal  $\alpha$  particles emitted by the source. The source beam is collimated using two aluminium targets and it interacts with the scattering foil positioned at the end of the support. The use of two independent detectors, each one with its own detection and monitoring system, constitutes a challenge with many technical issues to overcome, as we further discuss below, but after an opportune characterisation it is possible to successfully observe scattering events in a very wide interval of angles.

This phenomenon has been modelled with a Monte Carlo simulation written from scratch, which takes into account the complex geometry of the whole system and several first order corrections, such as straggling and nuclear charge screening effects. The results of the simulation are in good agreement with the experimental data in the interesting angular regions of the scattering distribution. In particular, the results obtained with ALPIDE detector are the ones more promising and interesting, enhanced by the fact that this is its first employment in an experiment like this.

**b. Technical issues** Most of the main technical issues have been faced when dealing with the necessity of a remote control of the apparatus. The first one involves the laboratory PC, which has an ancient operating system with outdated libraries. This results in the impossibility of running the detection system in an unique framework due to the ALPIDE detection system requirement for newer UNIX OS system and libraries. A temporary solution was found by using an Intel NUC Mini PC for the ALPIDE detection system, connected to the laboratory PC via a LAN built using a switch. This setup allows us to remotely control the system but only via a console. The graphical interface of the system can be controlled by desktop applications like TeamViewer, but the ladder requires an internet connection which would interfere with the ALPIDE communication protocol. Therefore, we introduce a second a second Intel Nuc Mini PC in the network in order to run the graphical application for remote control.

The final issue faced is the limitation imposed by the use of the CTRL port of ALPIDE, whose main purpose is not the data readout but only the monitoring of the detector itself. This limitation has been partially overcome by selecting an appropriate combination of the strobe and gap parameters.

**c. Possible experiment improvements** The main improvement that may be done to the apparatus is the replacement of the laboratory PC to a newer hardware with a recent OS system, with the necessity of a complete rewrite of the SSB acquisition system using newer libraries. This operation would drastically improve the maintainability of the system itself and also allow a second improvement, namely the integration of the ALPIDE detection system with the already existing interface for PicoScope. This would then allow to control the whole setup and the acquisition process from a single terminal a with less resources and efforts.

Another important improvement would be the possibility of using the faster port of the ALPIDE controller. In fact, the use of the CTRL port limits our acquisition rate to a maximum of 50 Hz. In order to use the faster port a firmware integration is needed alongside to a dedicated PCB able to support the readout operation. This would allow to extend the sensible time window of the controller, with the consequent increase of the maximum acquisition rate up to  $\sim 10$  kHz.

## REFERENCES

- [1] Pfeiffer Vacuum Technology AG, *HiCube Eco Turbo pumping stations*, [https://www.lesker.com/newweb/vacuum\\_pumps/pdf/manuals/hicube-eco-operating-manual.pdf](https://www.lesker.com/newweb/vacuum_pumps/pdf/manuals/hicube-eco-operating-manual.pdf)
- [2] Dipartimento di Fisica e Astronomia “Galileo Galilei”, *Sorgenti Radiogene*, [https://www.dfa.unipd.it/fileadmin/servtec/Sorgenti\\_polo\\_ott\\_2019.corretto.pdf](https://www.dfa.unipd.it/fileadmin/servtec/Sorgenti_polo_ott_2019.corretto.pdf)
- [3] Eckert & Ziegler, *Reference & Calibration Sources*, [https://www.ezag.com/fileadmin/user\\_upload/isotopes/isotopes/Isotrak/isotrak-pdf/Product\\_literature/EZIPL/EZIP\\_catalogue\\_reference\\_and\\_calibration\\_sources.pdf](https://www.ezag.com/fileadmin/user_upload/isotopes/isotopes/Isotrak/isotrak-pdf/Product_literature/EZIPL/EZIP_catalogue_reference_and_calibration_sources.pdf)
- [4] Laboratoire National Henri Becquerel, *Table de Radionucléides, Am-241*, [http://www.nucleide.org/DDEP\\_WG/Nuclides/Am-241\\_tables.pdf](http://www.nucleide.org/DDEP_WG/Nuclides/Am-241_tables.pdf)
- [5] AMETEK ORTEC, *Review of the Physics of Semiconductor Detectors*, [http://nuchem.iucf.indiana.edu/SiSpecs/SBD\\_det\\_cat.pdf](http://nuchem.iucf.indiana.edu/SiSpecs/SBD_det_cat.pdf)
- [6] Canberra Industries Inc, *Model 2003BT Silicon Surface Barrier Detector Preamplifier*, [https://mirion.s3.amazonaws.com/cms4\\_mirion/files/pdf/spec-sheets/c40680\\_2003bt\\_preamp\\_spec\\_sheet.pdf?1560277821](https://mirion.s3.amazonaws.com/cms4_mirion/files/pdf/spec-sheets/c40680_2003bt_preamp_spec_sheet.pdf?1560277821)
- [7] Canberra Industries Inc, *Model 2024 Fast Spectroscopy Amplifier*, [http://ohm.bu.edu/~pbohn/REPAIR\\_Advanced\\_Lab/Mossbauer/Data\\_Sheets/Model\\_2024\\_Super\\_Spec.pdf](http://ohm.bu.edu/~pbohn/REPAIR_Advanced_Lab/Mossbauer/Data_Sheets/Model_2024_Super_Spec.pdf)
- [8] Pico Technology Limited, *PicoScope 5000 Series*, <https://www.picotech.com/download/datasheets/PicoScope5000Series.pdf>
- [9] Milijenko Šuljić. *Study of Monolithic Active Pixel Sensors for the Upgrade of the ALICE Inner Tracking System*. Università degli studi di Trieste. A.A. 2016-2017.
- [10] ALICE ITS ALPIDE development team. *ALPIDE Operations Manual*. Ver. 0.3, July 2016
- [11] Xilinx. *7 Series FPGAs Data Sheet: Overview*. DS180 (v2.6.1) September 8, 2020
- [12] ARTY A7 board Documentation, <https://reference.digilentinc.com/reference/programmable-logic/arty-a7/reference-manual>
- [13] Gabriele Bortolato. *Sviluppo del firmware per il controllo del detector ALPIDE ed implementazione su FPGA*. Università degli studi di Padova. A.A. 2019-2020.
- [14] IPBus Documentation, <https://ipbus.web.cern.ch/ipbus/>
- [15] DE0-nano Cyclone IV Documentation, <http://www.terasic.com.tw/cgi-bin/page/archive.pl?Language=English&No=593&PartNo=4>
- [16] AlfaMC: a fast alpha particle transport Monte Carlo code, <https://arxiv.org/pdf/1211.5960.pdf>